Multipoint observation of fast mode waves trapped in the dayside plasmasphere

Kazue Takahashi,[1] John Bonnell,[2] Karl-Heinz Glassmeier,[3] Vassilis Angelopoulos,[4] Howard J. Singer,[5] Peter J. Chi,[4] Richard E. Denton,[6] Yukitoshi Nishimura,[7] Dong-Hun Lee,[8] Masahito Nosé,[9] and Wenlong Liu[10]

[1]   Multipoint observations of a dayside Pc4 pulsation event provide evidence of fast mode waves trapped in the plasmasphere (plasmaspheric cavity mode or virtual resonance). Time History of Events and Macroscale Interactions during Substorms (THEMIS)-A, the primary source of data for the present study, was moving outward near noon and detected poloidal oscillations, characterized by the azimuthal electric field component E_y and the radial and compressional magnetic field components B_x and B_z. The structure of the plasmasphere was constructed from the mass density radial profile estimated from the frequency of toroidal standing Alfvén waves observed at this spacecraft. The outer edge of the plasmapause (the maximum of the equatorial Alfvén velocity V_{Aeq}) was located at $L \sim 7$, and the minimum of V_{Aeq} was located at $L \sim 4$, forming a potential well structure required for mode trapping. Relative to the ground magnetic pulsations observed in the H component at a low-latitude station ($L = 1.5$), the E_y component exhibited a broad amplitude maximum around $L \sim 3.5$ and maintained a nearly constant phase from $L = 2$ to $L = 5$. In contrast, the B_z component exhibited an amplitude minimum and switched its phase by 180° at $L = 3.8$. This radial mode structure is consistent with theoretical models of mode trapping. Also, the E_y and B_z components oscillated ±90° out of phase, as is expected for radially standing waves.

Citation: Takahashi, K., et al. (2010), Multipoint observation of fast mode waves trapped in the dayside plasmasphere, *J. Geophys. Res.*, *115*, A12247, doi:10.1029/2010JA015956.

1. Introduction

[2] This paper presents observational evidence of fast mode trapping in the dayside plasmasphere in the Pc4 band (10–20 mHz). We adopt the term "trapping" from a his-

[1]Johns Hopkins University Applied Physics Laboratory, Laurel, Maryland, USA.
[2]Space Sciences Laboratory, University of California, Berkeley, California, USA.
[3]Institut für Geophysik und Extraterrestrische Physik, Technical University of Braunschweig, Braunschweig, Germany.
[4]Institute of Geophysics and Planetary Physics, University of California, Los Angeles, California, USA.
[5]National Oceanic and Atmospheric Administration/National Weather Service, National Centers for Environmental Prediction, Space Weather Prediction Center, Boulder, Colorado, USA.
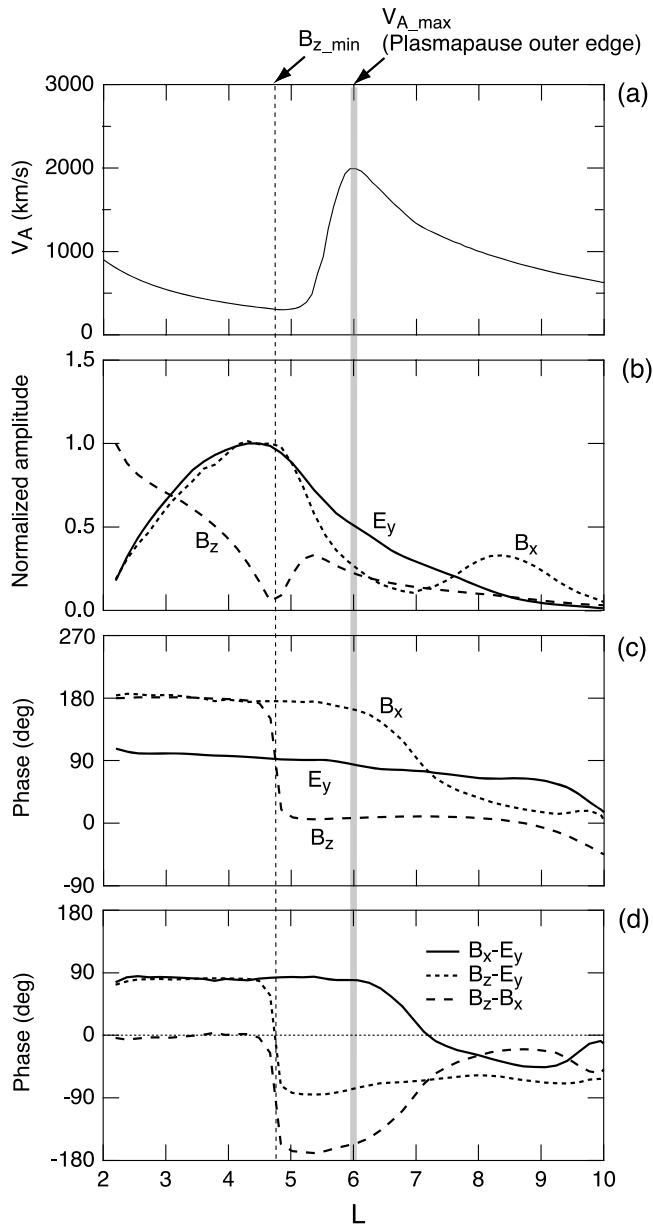[6]Department of Physics and Astronomy, Dartmouth College, Hanover, New Hampshire, USA.
[7]Department of Atmospheric and Oceanic Sciences, University of California, Los Angeles, California, USA.
[8]School of Space Research, Kyung Hee University, Yongin, South Korea.
[9]Data Analysis Center for Geomagnetism and Space Magnetism, Graduate School of Science, Kyoto University, Kyoto, Japan.
[10]Laboratory for Atmospheric and Space Physics, University of Colorado at Boulder, Boulder, Colorado, USA.

torical perspective of studies of magnetohydrodynamic (MHD) wave propagation in a structured magnetosphere [*Tamao*, 1978; *Yumoto and Saito*, 1983; see also *Turkakin et al.*, 2008] but with the intention of encompassing basically the same concepts investigated more recently as plasmaspheric cavity resonance [*Allan et al.*, 1986; *Yeoman and Orr*; 1989; *Zhu and Kivelson*, 1989; *Pekrides et al.*, 1997; *Leonovich and Mazur*, 2000a, 2000b; *Denton et al.*, 2002] or plasmaspheric virtual resonance [*Fujita and Glassmeier*, 1995; *Lee*, 1998; *Lee and Kim*, 1999; *Fujita et al.*, 2002]. Trapping occurs when a fast mode wave tunnels through a "potential barrier" into a trough of fast mode velocity (equaling Alfvén velocity V_A in cold plasmas) and then encounters a turning point. Mode trapping has been considered for waves with both low m (~1) [*Lee*, 1998; *Lee and Kim*, 1999; *Leonovich and Mazur*, 2000a, 2001; *Fujita et al.*, 2002] and high m ($\gg$1) [*Klimushkin et al.*, 2004; *Schäfer et al.*, 2007, 2008], where m is the azimuthal mode number. Our attention here is focused on plasmaspheric trapping of low-m waves.

[3] A major goal of ultra-low-frequency (ULF) wave research is to determine how the frequency of observed waves is established. On the one hand, we know very well that when subjected to impulsive or broadband disturbances, the magnetosphere responds by exciting standing shear Alfvén waves (field line resonance), the frequency of which

Figure 1. Radial structure of the fundamental plasmaspheric virtual resonance obtained in a dipole MHD simulation (modified from *Takahashi et al.* [2003]). (a) Equatorial Alfvén velocity assumed in the simulation. The velocity maximum V_{A_max} occurs at the outer edge of the plasmapause. (b) Amplitude of the poloidal components (E_y, B_x, and B_z) evaluated slightly north of the magnetic equator. The amplitude is normalized to the maximum value for each component. (c) Phase of E_y, B_x, and B_z. The phase values are defined by choosing the phase of B_z to be 180° at the inner edge ($L = 2$) of the simulation domain, taking into account the observed phase shift between the B_z component at THEMIS-A in the low-L region ($L < 4$) and the ground H component at the reference station LYFD ($L = 1.5$). (d) Cross phase for the three combinations of the poloidal components.

continuously varies with magnetic field line equatorial distance L [*Björnsson et al.*, 1971; *Poulter* and *Nielsen*, 1982; *Engebretson et al.*, 1986; *Denton et al.*, 2004]. On the other hand, ULF waves with L-independent frequencies are often observed, and they require other explanations. One such event (frequency ~2 mHz) observed on the dayside by the International Sun-Earth Explorer spacecraft as it moved from $L \sim 5$ to $L \sim 10$ motivated *Kivelson et al.* [1984] to develop a quantitative model of wave trapping in the whole magnetosphere (global cavity mode resonance) as a frequency-selection mechanism. Subsequent theoretical models incorporated the plasmasphere structure and resulted in numerical models of plasmaspheric cavity resonance or virtual resonance.

[4] Although many theoretical and numerical studies predicted plasmaspheric or global magnetospheric wave trapping, its occurrence in the real magnetosphere is not universally accepted. Complication arises when oscillations or waves external to the magnetosphere (driver waves) force the magnetic field and related quantities to oscillate at the frequency of the driving mechanism in a large volume within the magnetosphere. If the driver frequency is close to the predicted frequency of the trapped wave, interpretation of the observed wave phenomenon is not unique. Debates exist on which of these mechanisms controls the frequency. For example, multiharmonic Pc5 band pulsations have been attributed to both global cavity (or waveguide) mode [*Samson et al.*, 1992] and forcing by periodic changes in solar wind dynamic pressure [*Kepko et al.*, 2002]. Pi2 pulsations observed in the inner magnetosphere ($L < 6$) have been attributed to both plasmaspheric resonance [*Yeoman and Orr*, 1989; *Sutcliffe and Yumoto*, 1991; *Takahashi et al.*, 1995] and forcing by periodically generated sunward plasma flows in the magnetotail [*Kepko et al.*, 2001]. Pc4 waves observed on the dayside have been attributed to both driving by upstream waves [*Troitskaya et al.*, 1971; *Yumoto and Saito*, 1983; *Odera et al.*, 1991; *Le and Russell*, 1992; *Krauss-Varban*, 1994; *Vellante et al.*, 1996; *Howard and Menk*, 2001; *Heilig et al.*, 2007; *Clausen et al.*, 2009] and plasmaspheric mode trapping [*Kim et al.*, 1998; *Kim and Takahashi*, 1999; *Takahashi et al.*, 2009]. Both mechanisms might operate with a greater or smaller effect at different times. The key to detecting the trapped waves is observation of the spectral and spatial properties (i.e., the eigenmode structure) of the electric (**E**) and magnetic (**B**) fields of ULF waves in the likely trapping region.

[5] As a guide to data analysis, Figure 1 shows the radial structure of a fundamental virtual resonance mode obtained in a dipole MHD simulation [*Lee and Lysak*, 1999; *Takahashi et al.*, 2003]. In this simulation, the inner and outer boundaries are placed at $L = 2$ and $L = 10.5$, respectively, and the equatorial Alfvén velocity V_{Aeq} is given as shown in Figure 1a. A peak velocity occurs at $L = 6$, which corresponds to the outer edge of the plasmapause. Figure 1b shows the radial amplitude structure of the poloidal components, the eastward component of the electric field E_y, the radial component of the magnetic field B_x, and the compressional component of the magnetic field B_z, all evaluated slightly north of the magnetic equator and normalized to the respective peak amplitudes. The E_y and B_x components exhibit an amplitude peak at $L = 4.5$, with the amplitude remaining finite beyond the plasmapause, a property that

distinguishes the virtual resonance from an ideal cavity mode. The B_z component has an amplitude minimum at $L = 4.7$ near the location of the E_y maximum. Figure 1c shows that across the B_z minimum, the phase of B_z switches by ~180° while the phase of E_y remains constant, indicating that $L = 4.7$ is the standing wave node of B_z. The phase shift occurs over a finite radial distance analogous to shear standing Alfvén waves with finite ionospheric energy loss [*Newton et al.*, 1978]. Note that the phase of the oscillation is defined such that the phase of B_z is 180° at the inner boundary of the simulation, taking into account that we find a 180° phase shift between B_z and the ground H component at low latitude (see discussion in section 4.4 about this phenomenon). Figure 1d shows the relative phase between the three pairs of poloidal components in a format that can be easily compared with observations. These spatial mode properties should be observed if we have spacecraft equipped with **E** and **B** experiments and moving radially near the magnetic equator.

[6] In addition to the radial mode structure, the frequency of the trapped wave is an important parameter in testing the model against observations. An approximate frequency of the fundamental frequency of the trapped wave, f_{trap}, can be found from the time-of-flight (ToF) integral

$$f_{\text{trap}}^{-1} = 2R_E \int_{L_0}^{L_{\text{pp}}} dL/V_A, \tag{1}$$

where the integral is taken along the magnetic equator from the inner boundary L_0 to the plasmapause L_{pp}. Using the Alfvén velocity profile and adopting $L_0 = 2$ and $L_{\text{pp}} = 6$ as presented in Figure 1a, we get $f_{\text{trap}} = 7.5$ mHz. This value is very close to the numerically obtained virtual resonance frequency 8 mHz.

[7] In the past, many spacecraft were used to study ULF waves in the dayside magnetosphere, but none was quite capable of making sensitive measurements of both electric field and magnetic field on a single pass from well inside the plasmasphere ($L < 2$) to well outside the statistical plasmapause ($L > 7$) [*O'Brien and Moldwin*, 2003]. For example, *Schäfer et al.* [2007, 2008] studied the mode structure of plasmaspheric ULF waves observed with the Cluster satellites, but the high inclination of the spacecraft meant that only limited information on the radial mode structure was obtained. With the launch of the Time History of Events and Macroscale Interactions during Substorms (THEMIS) probes [*Sibeck and Angelopoulos*, 2008], our capability to detect ULF waves in the plasmasphere significantly improved. Each probe carries magnetic field and electric field experiments that are sensitive to oscillations with amplitudes below 1 mV/m and 1 nT, respectively. The probes are on low-inclination elliptical orbits, which include radial traversals of the inner magnetosphere near the magnetic equator. In addition, a large number of ground magnetometers provide a global monitor of ULF waves in conjunction with THEMIS observations.

[8] In this paper, we report a poloidal Pc4 event observed in the dayside magnetosphere on 21 June (day 173) 2008. The observations included simultaneous measurements of the interplanetary magnetic field (IMF) by the THEMIS-B probe, ULF waves and background plasma by the THEMIS-A probe that was moving radially outward in the dayside

magnetosphere, and magnetic field oscillations by the geosynchronous Geostationary Operational Environmental Satellite (GOES)-11 and GOES-12 satellites and ground magnetometers that were all longitudinally close to THEMIS-A. This observational configuration made it possible to separate spatial and temporal variations of ULF waves to a great degree. That is, we can determine the radial amplitude and phase structure of the Pc4 pulsations by comparing ULF waves at THEMIS-A to magnetic pulsations at other locations. We show that fast mode waves were present in the plasmasphere and that the waves had a radial amplitude and phase structure consistent with plasmaspheric mode trapping.

[9] The remainder of the paper is organized as follows. Section 2 describes the experiments used to acquire data used in the study, section 3 describes observations, section 4 presents discussion, and section 5 concludes the study.
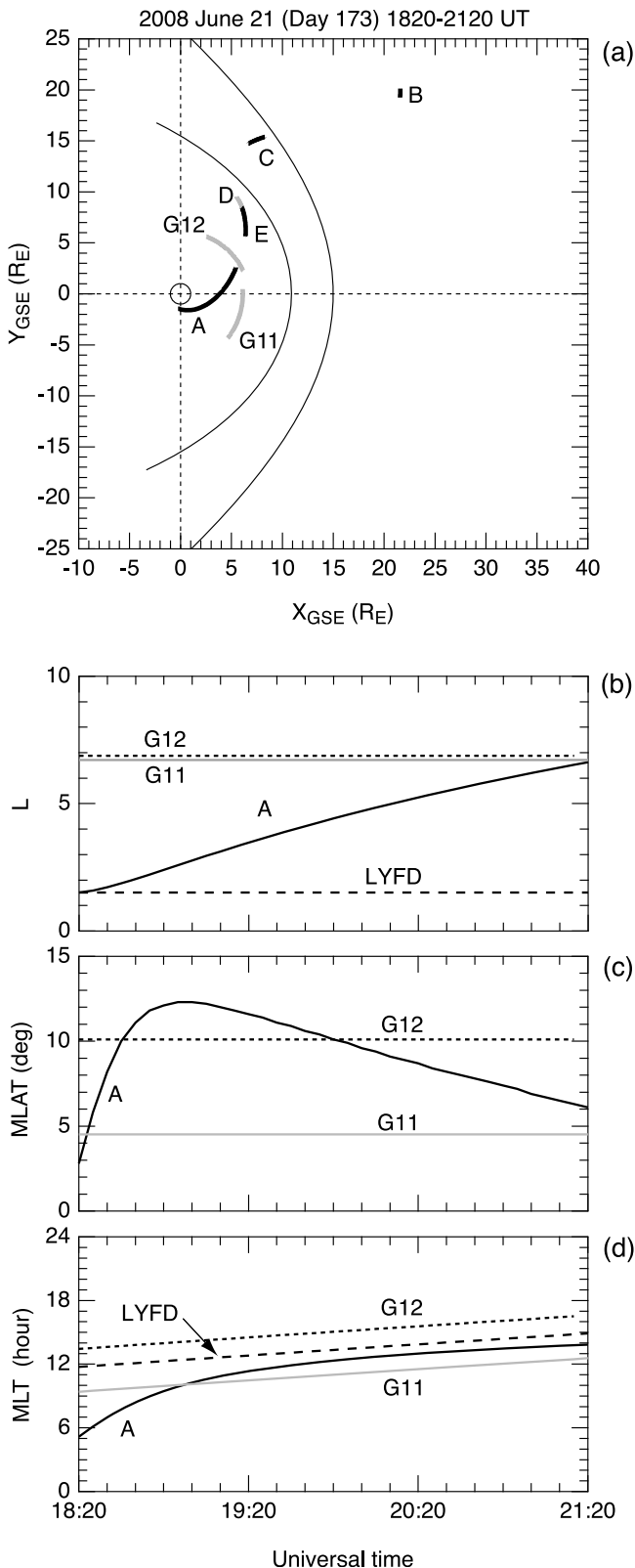
2. Experiments

[10] The core data for this study are **E** field [*Bonnell et al.*, 2008] and **B** field [*Auster et al.*, 2008] vectors measured by the THEMIS-A probe. The THEMIS data are supplemented by **B** field vectors measured in space by other THEMIS probes and the GOES-11 and GOES-12 geosynchronous satellites [*Singer et al.*, 1996] and measured on the ground at the Mid-continent Magnetoseismic Chain (McMAC) array (see http://spc.igpp.ucla.edu/mcmac/about.html), the THEMIS Education and Public Outreach (EPO) array [*Russell et al.*, 2008], and the Kakioka observatory (KAK) [*Tsunomura et al.*, 1994]. The THEMIS **E** field vectors are constructed from the two components measured in the satellite spin plane (approximately the geocentric solar ecliptic (GSE) X-Y plane). The **B** fields were measured by fluxgate magnetometers both in space and on the ground.

[11] We edited time series data from the different sources into files having common coordinates and time stamps. We first reduced the time resolution of **E** and **B** field data to 3.0 seconds by averaging the original high-time-resolution data (0.125 seconds for the **E** field data from THEMIS, 0.25 seconds for the **B** field data from THEMIS, and 0.5 seconds for the **B** field data from GOES and ground) in a common 3 second moving boxcar window. The only exception was THEMIS-B, from which only spin-fit (~3 seconds) data processed onboard were available. For THEMIS, the **B**·**E** = 0 condition was used to derive the third component of the electric field from the two components measured in the spacecraft spin plane. The spacecraft **E** and **B** field vectors are presented in a coordinate system referenced to the T89c model magnetic field [*Tsyganenko*, 1989], which we refer to as the model field-aligned (MFA) coordinates. In the MFA system, $\mathbf{e}_z$ is along the model magnetic field at the satellite, $\mathbf{e}_y$ (eastward) is parallel to $\mathbf{e}_z \times \mathbf{r}$, where **r** is the radial vector pointing from the center of the Earth to the satellite, and $\mathbf{e}_x$ (directed outward) completes a right-handed orthogonal system. The B_z component is essentially the same as the total component B_t at locations where the magnetic field model is valid.

[12] The spectral parameters that we derived from the **E** and **B** field data include power spectral density (PSD), coherence, and cross phase. The PSD of the field component i, $x_i(t)$, is given by $P_{ii}(f) = (2/T_{\text{window}})X_i(f)X_i^*(f)$, where T_{window} is the length of the data window and $X_i(f)$ is the

Fourier transform of $x_i(t)$, with t and f denoting time and frequency, respectively. The coherence and cross phase between components i and j are derived from the 2 by 2 spectral matrix $P_{ij}(f)$ following the standard definition found, for example, in *Bendat and Piersol* [1971]. All spectral parameters for the **E** and **B** fields were computed by using data segments from which the best fit second-polynomial was removed in order to suppress undesired power near zero frequency.

[13] Figure 2 shows the location of measurements during the interval of greatest interest to us: 1820 Universal Time (UT) to 2120 UT on 21 June (day of year = 173) 2008. THEMIS-A was mostly within ±2 hours of the magnetic noon meridian (Figures 2a and 2d) moving outward from $L = 1.5$ (perigee) to $L = 6.6$ (approximate geosynchronous distance) (Figures 2a and 2b). GOES-11 and THEMIS-A were longitudinally close to each other, with a local time separation of <2 hours except when THEMIS-A was closest to the Earth ($L \sim 1.5$; 1820–1835 UT). GOES-12 was ~4 hours east of GOES-11 and was in the postnoon sector for the entire period. The McMAC station Lyford (LYFD), which is used as the main reference location in character-izing the relative amplitude and phase of ULF waves observed elsewhere, also maintained a small longitudinal separation from THEMIS-A. We used McMAC data to examine the latitudinal dependence of ULF waves, and we used data from the other stations (KAK, EPO-Pine Ridge (PINE), and EPO-Loysburg (LOYS)) to examine the lon-gitudinal dependence.

[14] Figure 3 shows the location of measurements for the same 3 hour interval. In Figure 3, we use geomagnetic longitude and the L value as the coordinates to show the relative position between the ground stations and satellites. The magnetic coordinates were computed by using the dipole term of the International Geomagnetic Reference Field (IGRF)-11 model for epoch 2010 (available at http://wdc.kugi.kyoto-u.ac.jp/igrf/gggm/index.html).

3. Data

[15] This section presents data in the following order: First, we show observations in the solar wind, on the ground, and at geosynchronous orbit. These observations, made at a relatively constant location compared to the rap-idly moving THEMIS-A, provide information on the tem-poral variation of the IMF and magnetospheric ULF waves. We then examine the spectral properties and the **E-B** rela-tionship of the ULF waves detected by THEMIS-A and their dependence on radial distance. Finally, we examine the radial profile of the amplitude and phase of the ULF waves at THEMIS-A in a format that can be easily compared with the numerical model shown in Figure 1.

[16] Figure 4 shows the IMF measured by THEMIS-B (see Figure 2a for spacecraft location) and parameters derived from the IMF for 1800–2400 UT. In the GSE coordinates, the IMF had the largest component in the x direction (Figures 4a–4c), and its magnitude (B_t) was

Figure 2. THEMIS and GOES spacecraft position for 1820–2120 UT day 173 of 2008. The THEMIS probes are labeled by their respective alphabetical identification code. GOES-11 and GOES-12 are labeled G11 and G12, respec-tively. (a) Projection on the GSE coordinates *X-Y* plane. Schematic magnetopause and bow shock are shown. (b) Dipole *L*; LYFD is a McMAC station. (c) Dipole magnetic latitude; MLAT, magnetic latitude. (d) Dipole local time, LYFD also is included; MLT, magnetic local time.
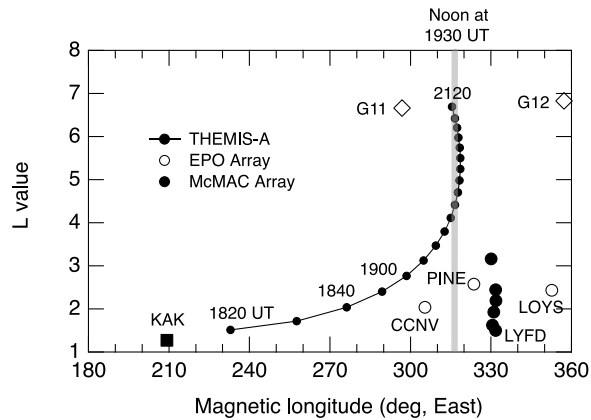
Figure 3. Geomagnetic longitude versus L positions of spacecraft and ground magnetometers used for the analysis of the Pc4 event on day 173 of 2008. The track of THEMIS-A covers the 3 hour interval shown in Figure 2. The thick vertical line indicates local noon at 1930 UT, which is the center of the 30 minute interval used to evaluate the longitudinal phase delay of the Pc4 waves (see Figure 7). Codes are shown for the stations used in the cross-spectral analysis: KAK (magnetic longitude = 209°E, L = 1.3), CCNV (magnetic longitude = 305°E, L = 2.0), PINE (magnetic longitude = 324°E, L = 2.7), LYFD (magnetic longitude = 332°E, L = 1.5), and LOYS (magnetic longitude = 353°E, L = 2.5).

~3 nT (Figure 4d). The IMF cone angle θ_{xB} ($= \cos^{-1}|B_{x\_GSE}/B_t|$) (Figure 4e) was mostly below 45° except during 2220–2330 UT. From ~1920 to ~1940 UT and from ~2130 to ~2230 UT, the cone angle became especially small (~10°) and THEMIS-B observed upstream ULF waves indicating that the spacecraft was magnetically connected to the bow shock and was in the region of ion beam instability [*Fairfield*, 1969]. In the first interval of small cone angle, B_{x_GSE} was positive throughout and B_{y_GSE} was mostly negative. With this field orientation, a parallel shock must have formed in the prenoon sector, and the upstream waves must have been most intense there [*Greenstadt and Olson*, 1976]. Figures 4f and 4g show dynamic spectra of B_{y_GSE} and B_t, respectively. The light trace included in Figures 4f and 4g is the theoretical frequency of the upstream waves $f_{uw} \approx 7.6B_t\cos^2\theta_{xB}$ given by *Takahashi et al.* [1984a]. This formula gives f_{uw} ~18 mHz except when the cone angle is large. During both of the two instances of strong upstream wave activity, the wave had a broad spectrum and was stronger in the transverse component. In the first burst (~1930 UT), the B_{y_GSE} power is present above the predicted frequency, whereas in the second burst (~2200 UT), the power is peaked near the predicted frequency. Therefore, there is some evidence that the upstream wave was capable of feeding Pc4 energy to the magnetosphere.

[17] We caution that the wave spectra at THEMIS-B may not reflect what is occurring near noon, which should be most relevant to ULF waves detected in the inner magnetosphere. In fact, the Pc4 pulsations detected on the ground and at geosynchronous orbit (shown in Figure 5) are more continuous than the upstream waves seen in Figure 4. We attribute the difference to the condition for detection of

strong upstream waves by a spacecraft in the solar wind: magnetic connection of the spacecraft to the quasi-parallel portion of the bow shock. That is, even when quasi-parallel shock is formed at the nose of the bow shock, a spacecraft may not observe strong upstream waves if the spacecraft is located away from the Sun-Earth line. We find in Figure 2 that THEMIS-B was ~20 R_E away from the Sun-Earth line,
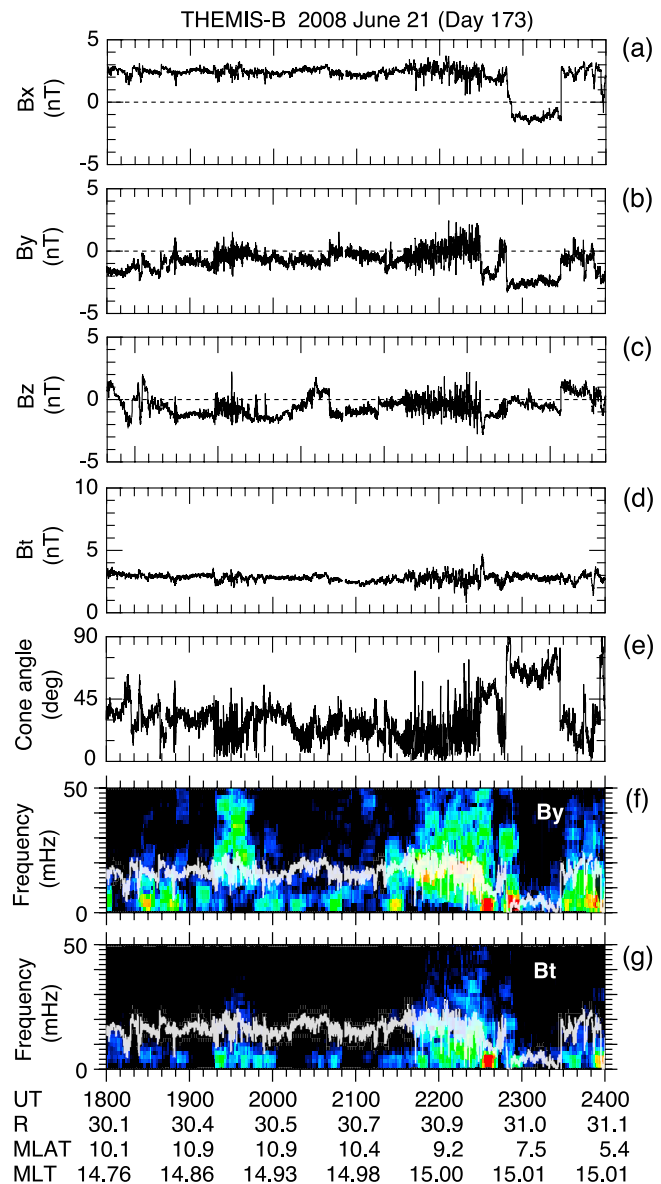
Figure 4. Magnetic field measured at THEMIS-B and derived parameters. The satellite location is given at the bottom in terms of geocentric distance R (R_E), dipole magnetic latitude (MLAT) (in degrees), and dipole magnetic local time (MLT) (in hours). (a–c) Vector components in the GSE coordinates. (d) Field magnitude. (e) Cone angle. (f) Dynamic spectrum of the B_y component. The range of the displayed power density is 0.5–50 nT²/Hz. The superimposed light trace indicates the theoretical frequency of the upstream waves given by *Takahashi et al.* [1984a]. (g) Same as Fiugre 4f except for the B_t component.
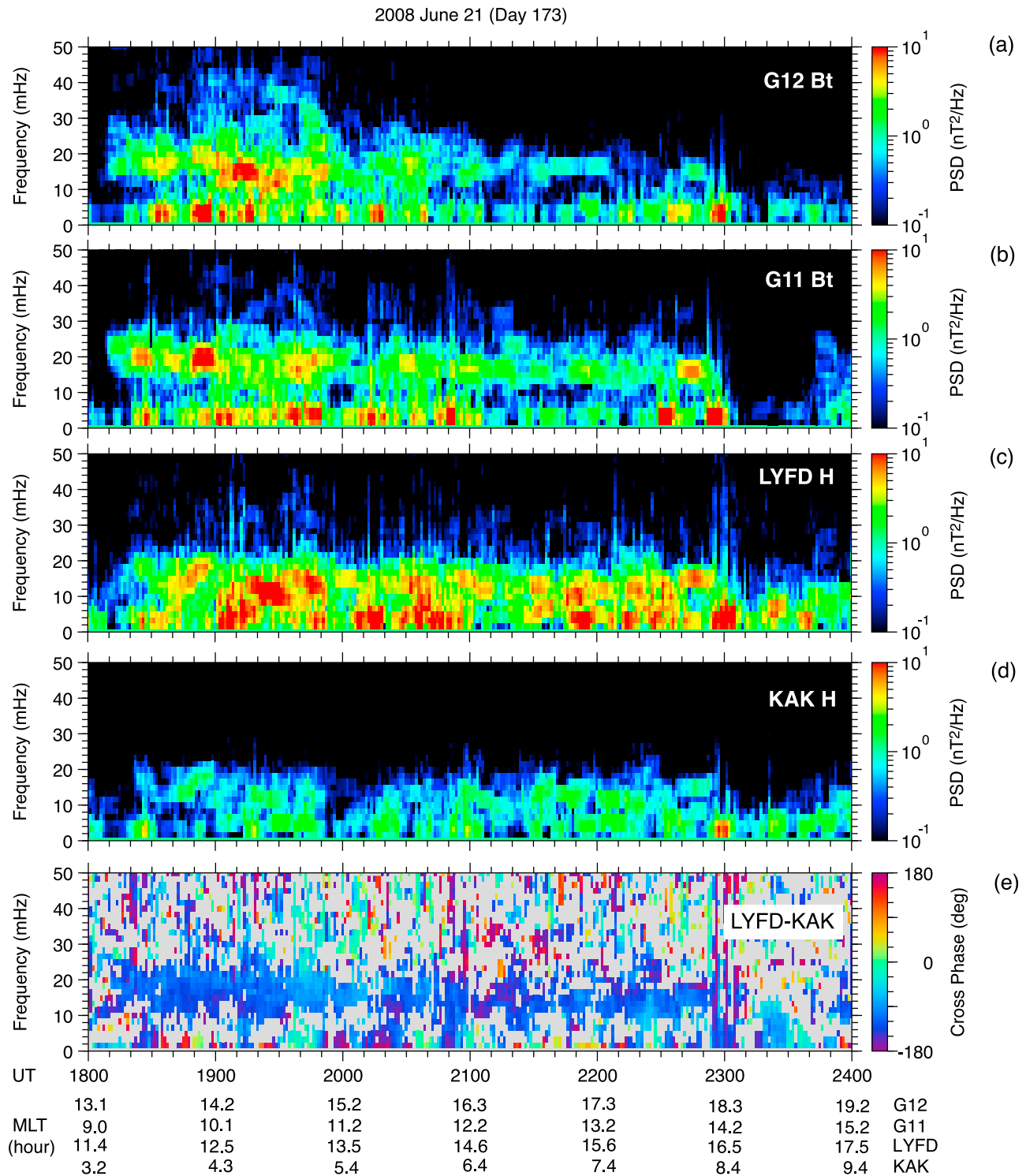
Figure 5. Spectral analysis of magnetic field data from GOES-11 and GOES-12 at geosynchronous altitude, and ground magnetometers at LYFD and KAK for a 6 hour period encompassing the continuous Pc4 activity of day 173 of 2008. A 600 second time window was shifted by 75 seconds in successive steps, with three point smoothing applied in the frequency domain. The magnetic local times of the satellite and ground stations are shown at the bottom. (a) PSD of the magnetic field total component B_t at GOES-12. (b) PSD of the B_t component at GOES-11. (c) PSD of the H component at LYFD. (d) PSD of the H component at KAK. (e) Phase of LYFD H relative to KAK H, displayed on a shaded background only when the coherence is >0.5.

which explains the sporadic appearance of upstream waves at this spacecraft.

[18] Figure 5 shows that Pc4 pulsations were present both in space and on the ground with amplitude and frequency properties as expected from the IMF condition shown in Figure 4. First, the power spectra of the B_t component at GOES-12 (Figure 5a) and GOES-11 (Figure 5b) and the H component at McMAC-LYFD (Figure 5c) and KAK (Figure 5d) indicate that there was continuous wave activity at all locations from 1810 to 2300 UT, the time interval of small cone angle found in Figure 4e. Second, the spectral peaks occur in the 10–30 mHz band, which covers the predicted frequencies of the upstream waves shown in Figures 4f and 4g. Although the spectral power at KAK is approximately one order of magnitude lower than at LYFD, the spectral shapes at both ground stations are quite similar, which implies that the waves propagated from the generation region near noon toward dawn and dusk. This long-range propagation is confirmed in Figure 5e as a band of high coherence that occupies the 10–20 mHz band and shows a nearly constant phase delay (~120°) at LYFD relative to KAK. From data shown in Figures 4 and 5, one might conclude that the Pc4 pulsations were just another example of simple propagation of upstream waves into the inner magnetosphere [Ponomarenko et al., 2005; Heilig et al., 2007; Clausen et al., 2009]. However, this interpretation becomes questionable as we examine the details of the wave spectrum at different locations and the physical properties of poloidal oscillations at THEMIS-A.

[19] Figure 6 shows the waveform and spectra of ULF pulsations in a 30 minute interval (1915–1945 UT) at six locations in space (THEMIS-B in the solar wind, THEMIS-C in the magnetosheath, THEMIS-D and THEMIS-E in the outer magnetosphere, and GOES-11 and GOES-12 at geosynchronous orbit) and seven locations on the ground (six McMAC stations and Kakioka). We show B_t in space and H on the ground because the former is an indicator of fast mode waves and the latter is usually the component that is most sensitive to ULF waves. On the ground, Pc4 pulsations with nearly identical waveforms were observed at all locations resulting in a spectral peak at 11 mHz. The wide latitudinal span of the pulsation is similar to those reported previously in the Pc3 and Pc4 bands [Ziesolleck et al., 1993; Yumoto et al., 1994; Feng et al., 1995; Takahashi et al., 2009]. Because the field line resonance frequency is strongly L-dependent, the observed L-independent frequency means that there was a mechanism other than field line resonance that determined the frequency of the ground Pc4 pulsations (according to the cross-phase analysis using neighboring pairs of McMAC stations, the fundamental field line resonance frequency at ~1930 UT was 43 mHz at $L = 2.1$ and 21 mHz at $L = 3.0$).

[20] From inspection of the spectra in space, it is evident that none of the pulsations detected at the spacecraft had a strong spectral peak at 11 mHz. At THEMIS-B, the spectrum is a power-law type and lacks a strong peak in the Pc4 band. The same can be said of the spectra at THEMIS-C, THEMIS-D, and THEMIS-E. This may not be surprising because these spacecraft were located in the postnoon sector, whereas the ground Pc4 pulsations were detected in the prenoon sector. Also, the IMF direction was such that a quasi-parallel shock was formed in the prenoon sector,

favoring upstream waves and ground Pc4 waves in that sector. In fact GOES-11 and GOES-12, which were closer to the McMAC array both in L and in longitude, detected spectral peaks that are stronger than at the other spacecraft. However, the spectral peaks at GOES-11 and GOES-12 both occurred at 17 mHz, higher than the frequency of the ground Pc4. Therefore, the ground observations cannot be explained by direct propagation of upstream waves from the solar wind to the outer magnetosphere and farther into the inner magnetosphere.

[21] The spectral mismatch between space and ground does not preclude solar wind energy source of the Pc4 pulsations. On the contrary, the pulsations had small m values consistent with large-scale disturbances coming from the solar wind. Figure 7 shows the coherence analysis of the 30 minute segment shown in Figure 6 using data from two pairs of ground stations: Carson City, Nevada (CCNV) and KAK on the left and PINE and LOYS on the right. In the time series plots (Figures 7a and 7e), data from stations closer to noon are shown at the top, and the cross phase (Figures 7d and 7h) is defined positive for propagation away from noon neglecting the $2n\pi$ ambiguities (see station location in Figure 3), where n is an integer.

[22] Figure 7d shows a cross-phase value of −106° at 11 mHz between CCNV (magnetic longitude = 305°E, $L = 2.0$) and KAK (209°E, $L = 1.3$). The negative cross phase means sunward propagation, which we consider unlikely. Therefore, we add 360° to this apparent phase value and get 254° (antisunward propagation). Dividing this by the longitudinal separation of the station, 96°, we get an m value of −2.6 (westward propagation), which is comparable to the m values reported on solar wind-driven Pc3-4 pulsations [Takahashi et al., 1984b]. Note that this derivation of m assumed that the phase did not depend on L at $L < 2.5$, which is the case according to the latitudinal phase variation observed along the McMAC array (data not shown).

[23] Figure 7e shows that the H component at PINE (324°E, 2.7) leads the H component at LOYS (353°E, 2.5) by ~9 seconds. This means that the pulsations propagated eastward (antisunward) at an apparent ground velocity of ~200 km/s. In the cross-phase spectrum, this delay appears as an ~34° phase shift (at 11 mHz), which translates to $m \sim$ 1.2. Because the longitudinal separation between PINE and LOYS is only 29°, we believe there is no $2n\pi$ ambiguity in the cross phase.

[24] Having established the global nature of the Pc4 wave on the ground, we now examine data from THEMIS-A. Figure 8 shows an overview of ULF waves at THEMIS-A during 1820–2120 UT. The wave activity is represented by dynamic spectra of the five field components over the frequency of 0–100 mHz (E_z is not shown because it is zero by definition when we derive the **E** field vector from two-dimensional measurements). The location of the spacecraft is shown at the bottom using coordinates based on a centered dipole.

[25] The most prominent feature in Figure 8 is the strong wave power in E_y and B_x that appears in the 5–25 mHz band for much of the 3 hour interval (stronger in the first half). The additional presence of B_z power means a compressional mode. The intensity of the wave is highest from 1920 UT ($L \sim 3.5$) to 1950 UT ($L \sim 4.5$). Other components also exhibit similar enhancements but with lower spectral intensity and
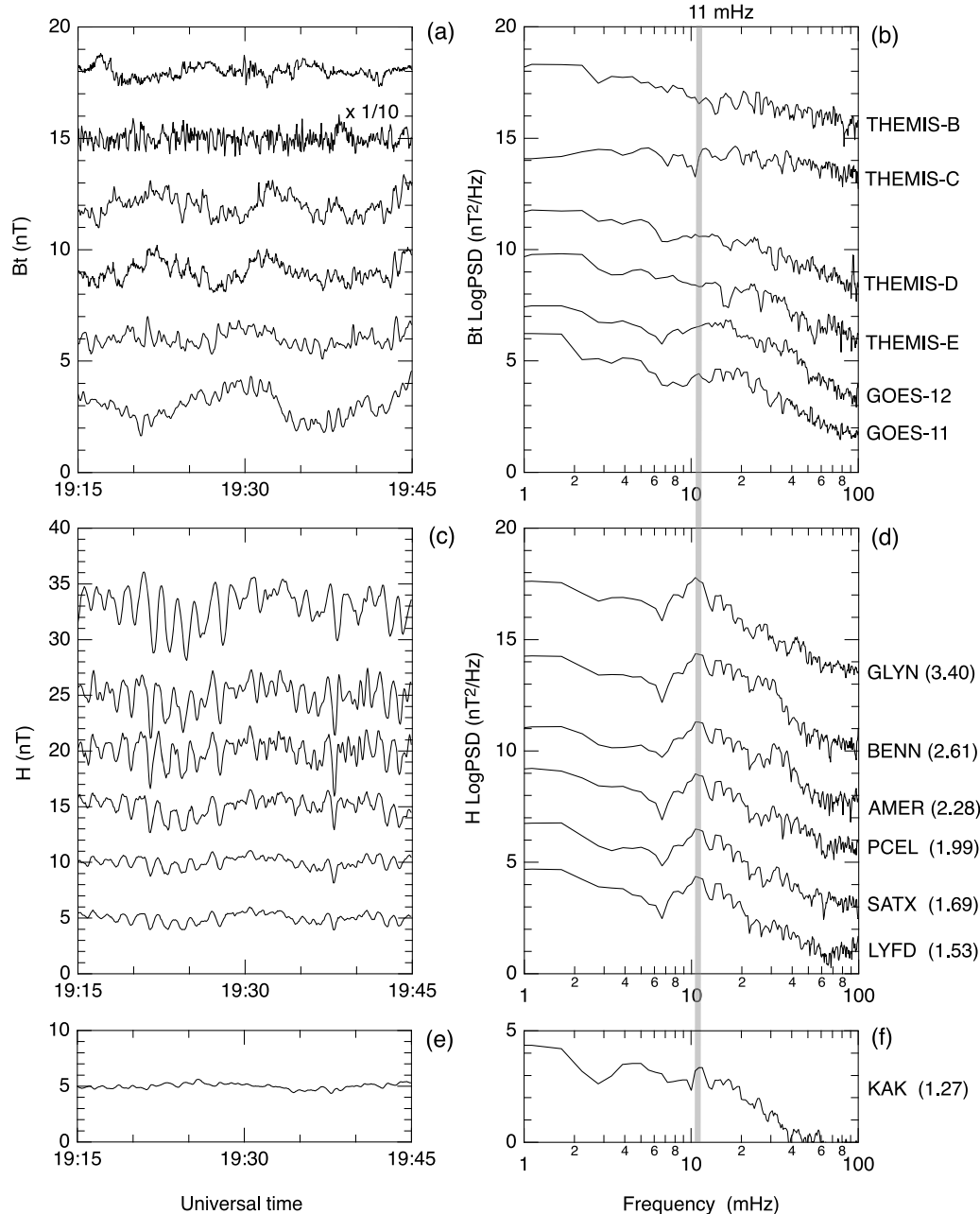
Figure 6. Comparison of ULF pulsations observed in space and on the ground during a 30 minute period on day 173 of 2008. (a) Time series of the magnetic field magnitude B_t in space. (b) Power spectra of the spacecraft data. (c) Time series of the H component at six McMAC stations. (d) Power spectra of the McMAC data. Station L values are shown in parentheses. The vertical line marks the spectral peak at 11 mHz. (e) Time series of the H component at KAK. (f) Power spectrum of the KAK data.

some additional spectral features. The dominance of the E_y, B_x, and B_z components means that the field line motion was primarily in the radial direction and accompanied compression; for that reason, we identify the oscillations as (compressional) poloidal mode.

[26] In addition to the poloidal oscillations, multiharmonic toroidal waves were present. The signature of the toroidal waves is the falling tones that appear in the E_x and B_y spectra, most clearly from 1900 to 1940 UT. The funda-

mental frequency of the toroidal waves is in the 10–20 mHz band at the time when the toroidal waves are strongest. Toroidal-poloidal mode coupling [*Zhu and Kivelson*, 1989; *Lee and Lysak*, 1989] is a likely explanation of the simultaneous appearance of the two polarization modes.

[27] As we stated in the introduction, the radial plasma density structure controls wave trapping. To determine whether trapping was possible, we estimated the equatorial mass density and the corresponding Alfvén velocity using a

2008 June 21 (Day 173)
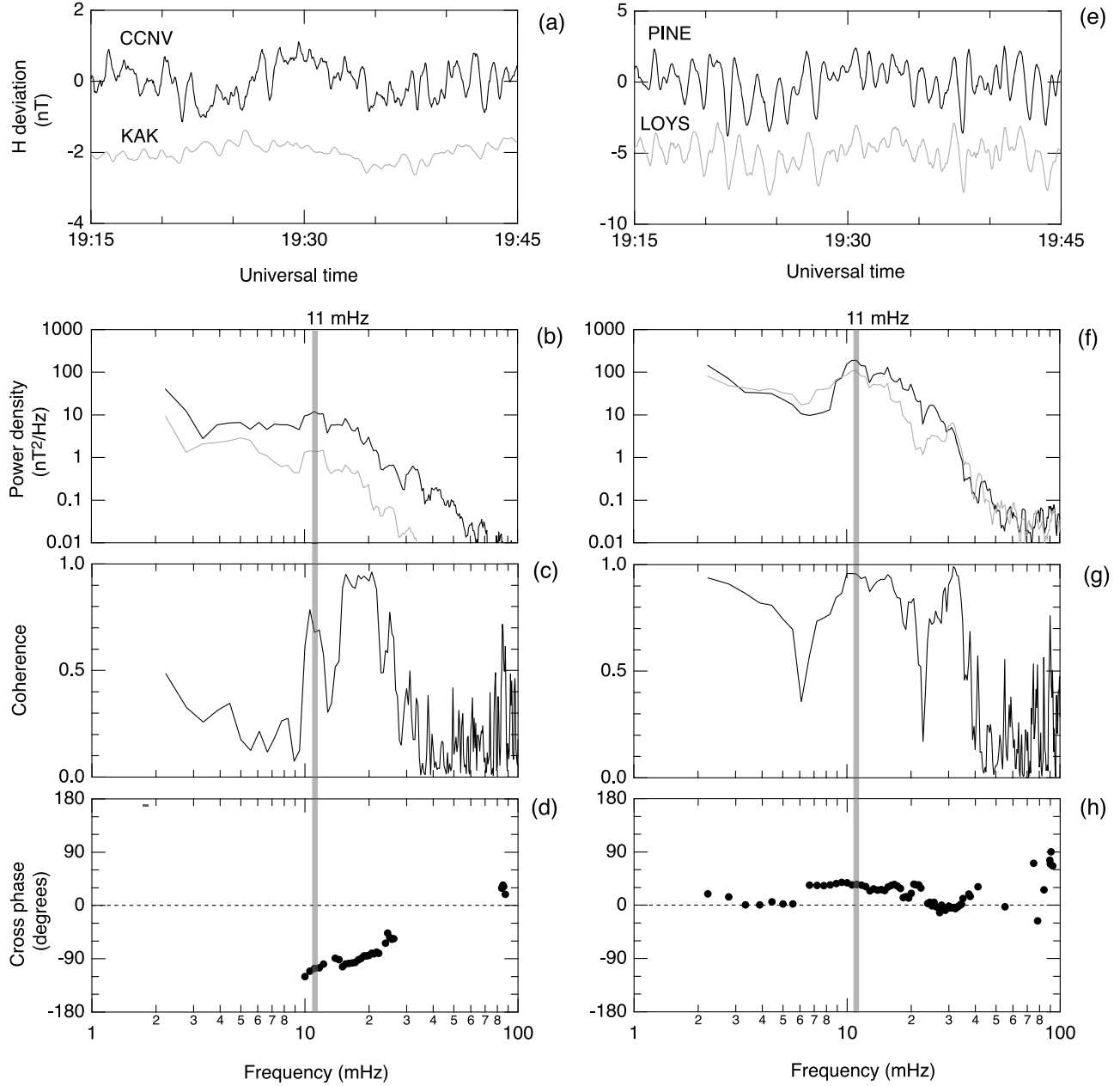
Figure 7. Waveform and spectral properties of ground *H* components from longitudinally separated sites for the time interval of 1915–1945 UT on day 173 of 2008. The left column shows the combination of CCNV and KAK, and the right column shows the combination of PINE and LOYS. (a, e) Time series plots of the *H* components. (b, f) Power spectra. The vertical line marks the spectral peak at 11 mHz. (c, g) Coherence. (d, h) Phase of *H* at the first station (shown as a black curve in Figures 7a and 7e) relative to the phase of *H* at the second station (shown as a shaded curve in Figures 7a and 7e). Cross phase is shown if coherence is >0.5.

magnetoseismic technique that we developed in recent years [see *Takahashi et al.*, 2010, and references therein]. In this technique, we determine the equatorial mass density from the observed frequencies of toroidal waves by solving the standing Alfvén wave equation of *Singer et al.* [1981],

$$\mu_0 \rho \frac{\partial^2 (\xi_i / h_i)}{\partial t^2} = \frac{1}{h_i^2} \mathbf{B}_0 \bullet \nabla \{ h_i^2 [\mathbf{B}_0 \bullet \nabla (\xi_i / h_i)] \}, \quad (2)$$

where ρ is plasma mass density, $\mathbf{B}_0$ is the background magnetic field, ξ_i is field line displacement, and h_i is a scale factor proportional to the separation of field lines that define the direction of field line displacement.

[28] The equation allows use of any geomagnetic field model; in the present application, we used the TS05 external magnetic field model [*Tsyganenko and Sitnov*, 2005] coupled with the internal magnetic field model IGRF (available
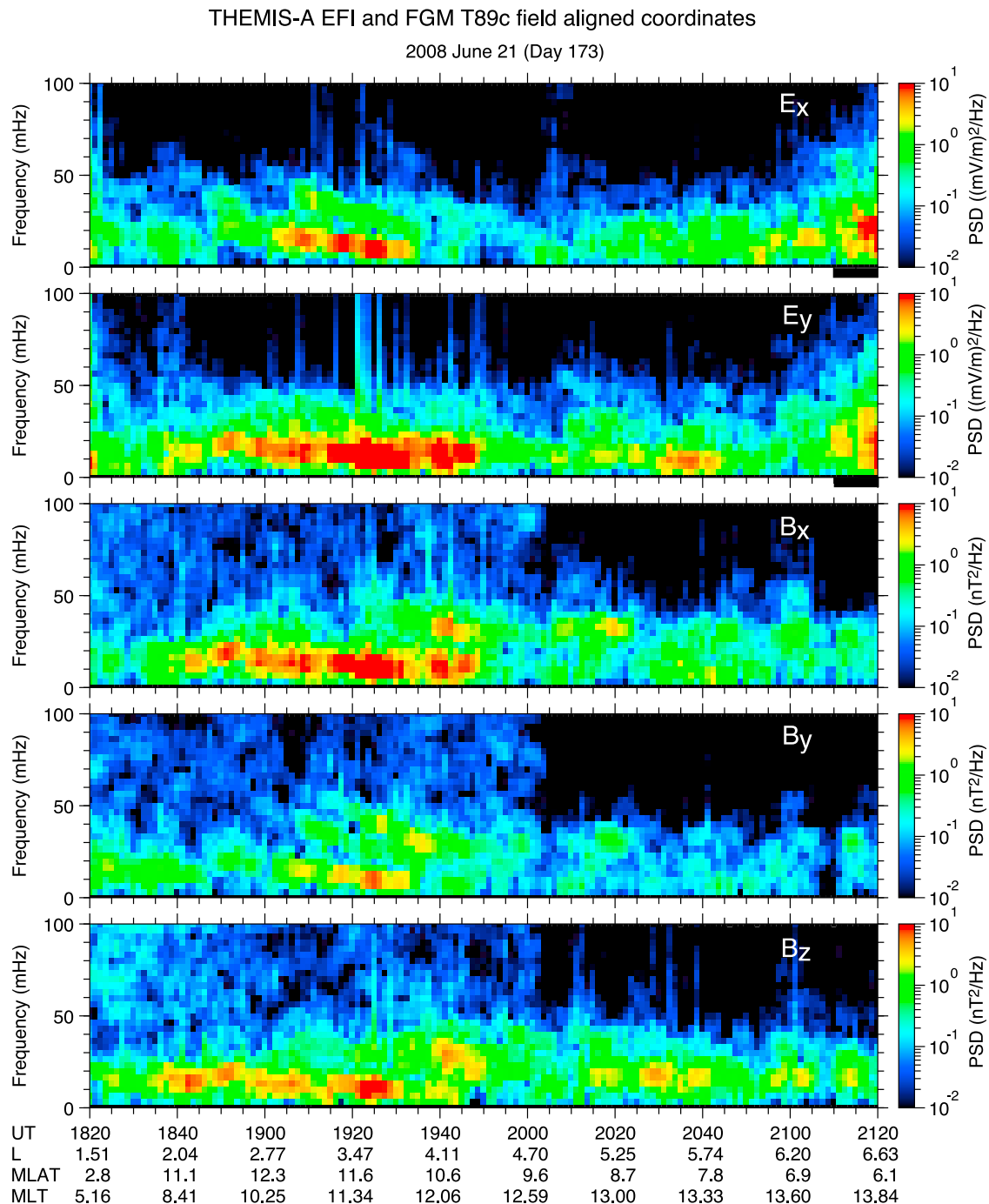
Figure 8. Dynamic spectra of the electric and magnetic fields measured at THEMIS-A. A 300 second time window was shifted by 75 seconds in successive steps, with three point smoothing applied in the frequency domain. The black bar on the time axis for E_x and E_y indicates possible contamination by satellite wake. The satellite position is shown at the bottom.

at http://www.ngdc.noaa.gov/IAGA/vmod/igrf.html). The field line mass density variation, which also needs to be specified, was assumed to be a power-law function

$$\rho = \rho_{eq}(LR_E/R)^\alpha, \qquad (3)$$

where ρ_{eq} is the equatorial mass density and R is geocentric distance to a point on the field line. *Denton et al.* [2006] and *Denton* [2006] summarize our state of knowledge about the

field line distribution of magnetospheric mass density. For $L > 6$, they recommend $\alpha = 1$, and for $L = 4$–6, they recommend $\alpha = 2$. There is little information about the field line dependence for lower L values; however, ground-based results [*Menk et al.*, 1999; *Price et al.*, 1999] indicate that the field line dependence may be steeper for such L values, presumably because of ionospheric mass loading. On the basis of such results, it would be reasonable to assume a model for which α varies from 1 at $L = 6$, to 2 at $L = 4.5$, to 4 at $L = 3.5$,

and to 6 at $L = 2$. This dependence can be reasonably well modeled by a function such as $\alpha = 0.225L^2 - 3.05L + 11.25$. We use that model here for $\alpha(L)$.

[29] Figure 9 shows the toroidal frequencies and derived parameters at THEMIS-A for the time interval 1820–2240 UT, all plotted as a function of the dipole L value at THEMIS-A. The toroidal frequencies (Figure 9a) were determined by visual inspection of the power spectra of the E_x and B_y components computed in 10 minute data windows. The fundamental through fourth harmonics were visible at some point in
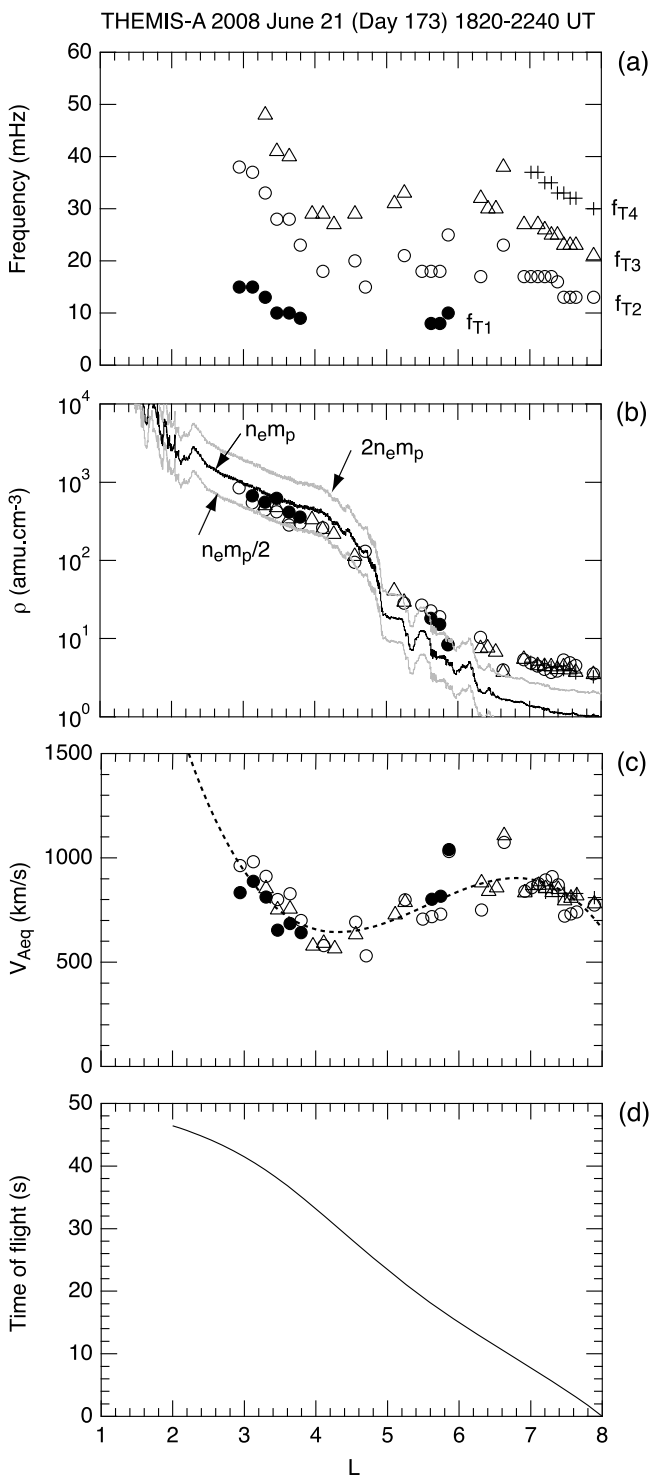
the interval examined. The frequencies decreased as a function of L in the low L (2–4) and high L (6–8) regions, but they increased in between.

[30] Figure 9b shows the mass density ρ at the spacecraft estimated from each measurement of toroidal frequency and plotted by using the same markers used in Figure 9a. The density decreased from ~900 amu.cm^{-3} at $L = 3$ to ~3 amu.cm^{-3} at $L = 8$, with a large rate of decrease at $L = 4$–6. This region is identified as the plasmapause. Also plotted in Figure 9b is a continuous curve labeled $n_e m_p$, where m_p is the proton mass and n_e is the electron number density at the spacecraft that was estimated from the spacecraft potential [*Mozer*, 1974; *Li et al.*, 2010]. The thin shaded curves represent factor-of-two margins of error for the estimated n_e. We would expect $\rho = n_e m_p$ for H$^+$ plasma and $\rho > n_e m_p$ for plasma containing heavy ions (i.e., He$^+$ and O$^+$). At $L < 4.5$, $n_e m_p$ is very close to ρ, which implies that protons were the major ions in the plasmasphere. The ρ values lower than $n_e m_p$ are unphysical because no ions are lighter than protons. However, the difference is within the error margins. (When we assume $\alpha = 1$ for all L, we get slightly higher mass density at $L < 4$, but most estimated values still lie below $n_e m_p$.) At $L > 4.5$, the reverse, $\rho > n_e m_p$, occurs. In this case, ρ is greater than $n_e m_p$ by a factor of 3–4, a result that definitely requires the presence of heavy ions. Previous studies reported an increase in heavy ion densities outside of the plasmasphere [*Fraser et al.*, 2005; *Takahashi et al.*, 2006], and our THEMIS-A result is another example of the L dependence of ion composition. The important facts here are that heavy ions outside $L \sim 4$ make the mass density plasmapause a more gradual structure than the electron plasmapause and that we cannot use $n_e m_p$ as a proxy of ρ in investigating MHD propagation in the magnetosphere.

[31] Figure 9c shows the equatorial Alfvén velocity V_{Aeq} calculated by using the estimated mass density and the equatorial magnetic field intensity given by the TS05 model. The smooth dashed curve is a third-order polynomial fitted to the V_{Aeq} data points. The polynomial exhibits a minimum of 640 km/s at $L = 4.3$ and a maximum of 900 km/s at $L = 6.8$, qualitatively similar to the model shown in Figure 1a but with a much smaller peak-to-trough ratio. From the V_{Aeq} profile, we calculated the fast mode propagation time (ToF) along a radial path from $L = 8$ to $L = 2$, and the result is shown in Figure 9d. To estimate the frequency of the

THEMIS-A 2008 June 21 (Day 173) 1820-2240 UT

Figure 9. Parameters derived from the toroidal waves observed by THEMIS-A during 1820–2240 UT on day 173 of 2008. All parameters are plotted as a function of dipole L. (a) Toroidal frequencies at the fundamental (f_{T1}) through fourth (f_{T4}) harmonics. (b) Mass density at the spacecraft estimated from the toroidal frequencies (shown by different markers) and plasma mass density defined by $n_e m_p$, where m_p is the proton mass and n_e is the electron number density at the spacecraft estimated from the spacecraft potential. Shaded traces show the upper and lower error limits of $n_e m_p$. (c) Equatorial Alfvén velocity corresponding to the mass density estimated from the toroidal frequencies. The smooth dashed curve is the third-order polynomial fitted to the velocity estimates. (d) Fast mode wave equatorial ToF calculated using the smooth curve in Figure 9c for radial inward propagation from $L = 8$.

trapped wave by using the ToF equation (1), we take the outer boundary at $L = 6.8$, where V_{Aeq} shows a peak value associated with the plasmapause, and the inner boundary at $L = 3.0$, where the velocity matches the peak value 900 km/s (making this location a nominal turning point). There are no data points for $L < 3$ since toroidal mode power was absent there. The peak velocity of 900 km/s coincides with the first toroidal mode waves power observed (at $L = 3$). The ToF values are 41 s at $L = 3.0$ and 9 s at $L = 6.8$, which give $f_{trap} = 16$ mHz. This frequency falls right into the 10–20 mHz band of the observed Pc4 pulsations and makes mode trapping a viable mechanism in terms of frequency.

[32] Having confirmed the presence of an Alfvén velocity minimum (or potential well structure) that is required for plasmaspheric wave trapping, we now examine the **E** and **B** data for signature of mode trapping. Figure 10 shows the time series and spectra of five selected field components, B_z at GOES-11; E_y, B_x, and B_z and at THEMIS-A; and H at LYFD for two 15 minute intervals, 1915–1930 UT and 2015–2030 UT. THEMIS-A was at $L = 3.3–3.8$ during the first interval and at $L = 5.1–5.5$ during second interval. Both intervals were within the Alfvén velocity "potential well" according to Figure 9c.

[33] In the first interval (Figures 10a and 10b), there is evidence of trapped poloidal waves. First, all field components except GOES-11 B_z oscillated at a common frequency of 11 mHz, indicating that a fast mode oscillation was present in the plasmasphere and that the oscillation propagated to the ground. The E_y, B_x, and B_z components at THEMIS-A had peak-to-peak amplitude reaching 2.5 mV/m, 1.7 nT, and 1.5 nT, respectively. The H component at LYFD had peak-to-peak amplitude reaching 1.3 nT, comparable to B_z at THEMIS-A. Second, following the vertical dashed lines drawn through the peaks of E_y, we see a constant phase delay among the field components at THEMIS-A. Most importantly, E_y lagged B_z by 21 or 24 seconds (the time resolution of the data is 3 seconds), which corresponds to a quarter of the wave period 90 seconds, or ~90° in cross phase. This phase delay means that the fast mode oscillation was standing in the radial direction. A radially propagating wave should have exhibited a phase delay of 0° or 180° between E_y and B_z. Meanwhile, the B_x and B_z components oscillated in phase, which implies that the oscillation was standing in the z direction as well. Because the spacecraft was located above the magnetic equator, the field line displacement is inferred to be symmetric about the magnetic equator, which is evidence of a fundamental standing mode along the field line (see the cavity mode schematic by *Takahashi et al.* [1995, Figures 16 and 17]). The ground H component lagged E_y by ~90° and had a phase delay of ~180° with respect to B_z. Much weaker magnetic oscillation was observed at GOES-11 than at THEMIS-A or on the ground, and the spectral power at GOES peaked at 18 mHz instead of 11 mHz.

[34] In the second interval (Figures 10c and 10d), the oscillation differed significantly among the field components. Whereas E_y and H (but not B_x) oscillated at the same frequency (13 mHz) and appear to have maintained a cross phase similar to that observed in the first interval (but with lower amplitudes), the B_x and B_z components at THEMIS-A oscillated at a higher frequency (18 and 32 mHz for B_x and 18 mHz for B_z). This implies that although there were os-

cillations in space at multiple frequencies, only the 13 mHz oscillation propagated to the ground. (We recognize that the waveform changed within the 15 minute interval and thus the spectral content for a given instance needs to be discussed with caution.) A possible reason for the absence of a 13 mHz oscillation in B_x is that the radial mode structure differed between E_y and B_x. In the simulation result shown in Figure 1b the mode structure is similar between E_y and B_x at $L < 5$ but is quiet different at larger L. The B_x component has a quasi-node at $L \sim 7$ where the amplitude is minimum and phase changes rapidly. It is possible that THEMIS-A was located close to the quasi-node.

[35] The spectral peaks at 18 mHz and 32 mHz seen in Figure 10d merit brief discussion. We attribute the 18 mHz spectral peak to upstream waves, because a peak is seen in the spectrum of the GOES-11 B_z component at the same frequency and because the predicted frequency of the upstream waves is also ~18 mHz (see Figure 4g). We infer that as THEMIS-A moved outward, it approached the source region of the 18 mHz waves and detected them with appreciable amplitude. This scenario, however, is not perfect since we cannot explain why an 18 mHz oscillation was absent in the E_y component (a radially propagating fast mode wave should have accompanied an azimuthal electric field perturbation). The 32 mHz oscillation seen in the B_x component likely came from a guided poloidal mode [*Radoski*, 1967]. According to Figure 9a, the third harmonic of the toroidal oscillations occured at ~30 mHz around the time the 32 mHz oscillation was detected in B_x. Since a guided poloidal wave and a toroidal wave excited on a common field line have nearly identical frequencies at high-order harmonics [*Cummings et al.*, 1969], we infer that the poloidal oscillation was excited at the third harmonic. A recent satellite study by *Schäfer et al.* [2007] reported excitation of third harmonic poloidal waves near the plasmapause, so the third harmonic is not unique to our data.

[36] In general, the amplitude of magnetospheric ULF waves is strongly time modulated, often making it difficult to determine whether the amplitude variation seen from a spacecraft is spatial or temporal. An effective way to minimize the temporal variations is to use ULF waves observed in a fixed point in space or on the ground as a reference in characterizing the properties of the waves detected elsewhere in space. This has been successfully done in studies of Pi2 pulsations [e.g., *Takahashi et al.*, 2003], and now we apply it to the present Pc4 event.

[37] As a demonstration of how this approach works, Figure 11 dynamically displays spectral parameters generated from the poloidal components (E_y, B_x, and B_z) at THEMIS-A and H at LYFD. The PSD of these components (Figures 11a–11d) indicates a strong temporal variation of pulsation intensity both in space and on the ground. However, once we compute the cross phase for the pairs of E_y-H (Figure 11e), B_x-H (Figure 11f), and B_z-H (Figure 11g), shown only if coherence is >0.5 on the shaded background (coherence <0.5), we find a strong connection between the field oscillations at THEMIS-A and LYFD. The ground-satellite coherence is persistently high in the 10–20 mHz band for most of the 3 hour interval shown, indicating that there was a wave mode in space that occupied the L range of 1.5–6.6 (and perhaps beyond) and propagated to the ground station located at $L = 1.5$.
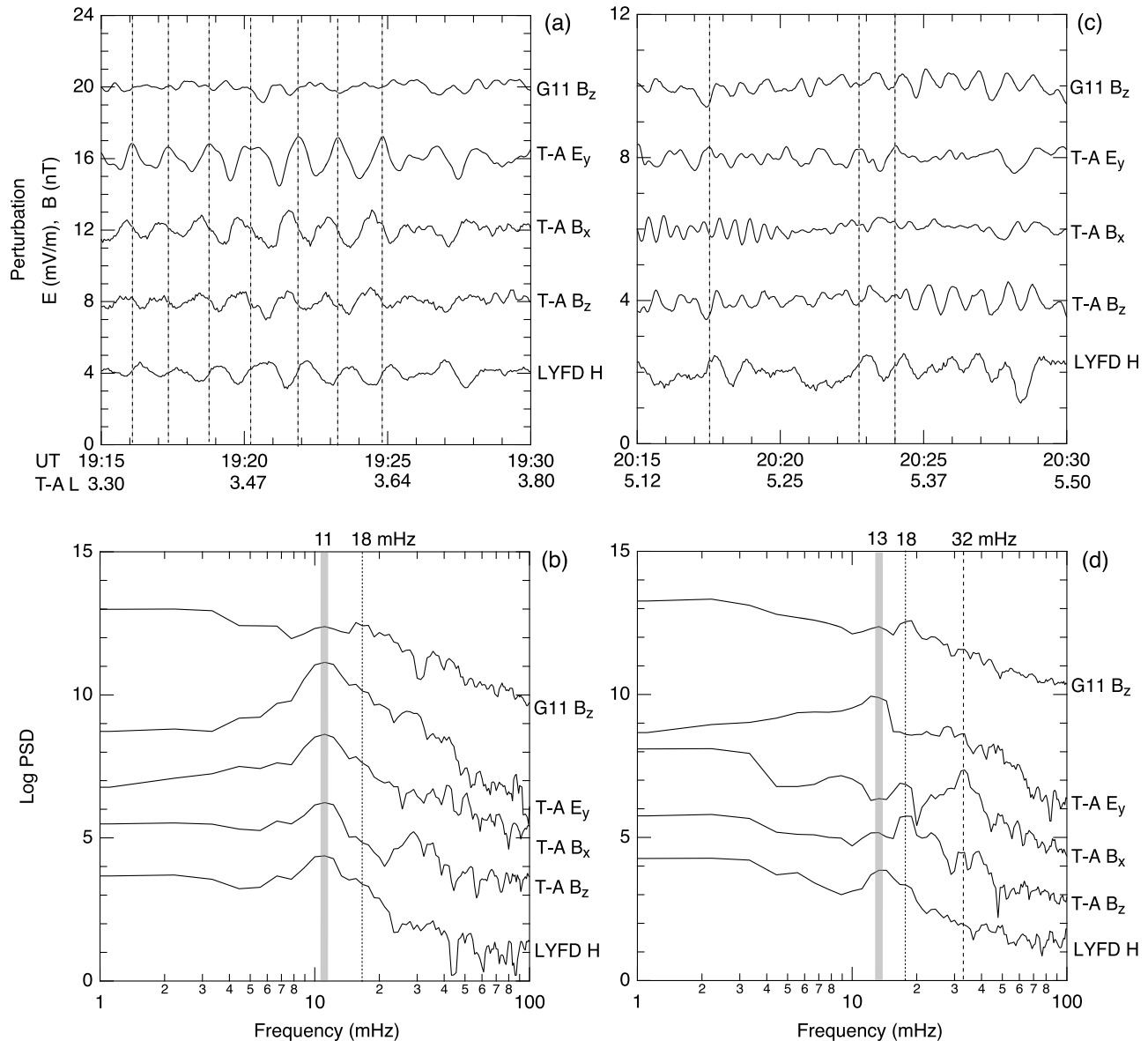
Figure 10. (a, c) Waveforms and (b, d) spectra of selected field components for two 15 minute intervals during the Pc4 event on day 173 of 2008. In the time series plots, data were high-pass filtered by removing 300 second running averages, and vertical dashed lines are drawn through the peaks of the E_y component. In the spectrum plots, vertical lines are drawn through the dominant peaks. The L value of THEMIS-A (T-A L) is shown at the bottom of the waveform plots.

[38] In addition, it is obvious that there is a clear difference among the three field components at THEMIS-A in the L dependence of the phase. The E_y-H cross phase (Figure 11e) is nearly constant at ~90° (dark orange), from 1830 UT ($L \sim 1.7$ at THEMIS-A) to 2040 UT ($L \sim 5.7$). This confirms that the E_y-H phase delay seen in the time series plots of Figure 10 is a persistent feature. The B_x-H cross phase (Figure 11f) also shows a nearly constant phase over a similar time span, but at ~180°. The B_z-H cross phase (Figure 11g) exhibits a rapid change at ~1940 UT ($L \sim 4$). Prior to this instance, the cross phase appears in purple, meaning an ~180° phase delay; after ~1940 UT, the color changes to light green (~0° phase delay).

[39] A more quantitative description of the amplitude and cross phase is possible by integrating the spectral parameters over a frequency band. Figure 12 shows the raw amplitude (top row), normalized amplitude (second row), coherence (third row), and cross phase (fourth row) of E_y (left column), B_x (center column), and B_z (right column) at THEMIS-A relative to H at LYFD. These parameters were obtained by integrating the spectral matrix $P_{ij}(f)$ over 10–20 mHz. The data window is 600 seconds long and is moved forward in 75 second increments. The amplitude is defined to be the square root of the integrated PSD. If the magnitude of $P_{ij}(f)$ is peaked at a frequency within the selected band, the wave properties at that frequency will determine the value of the
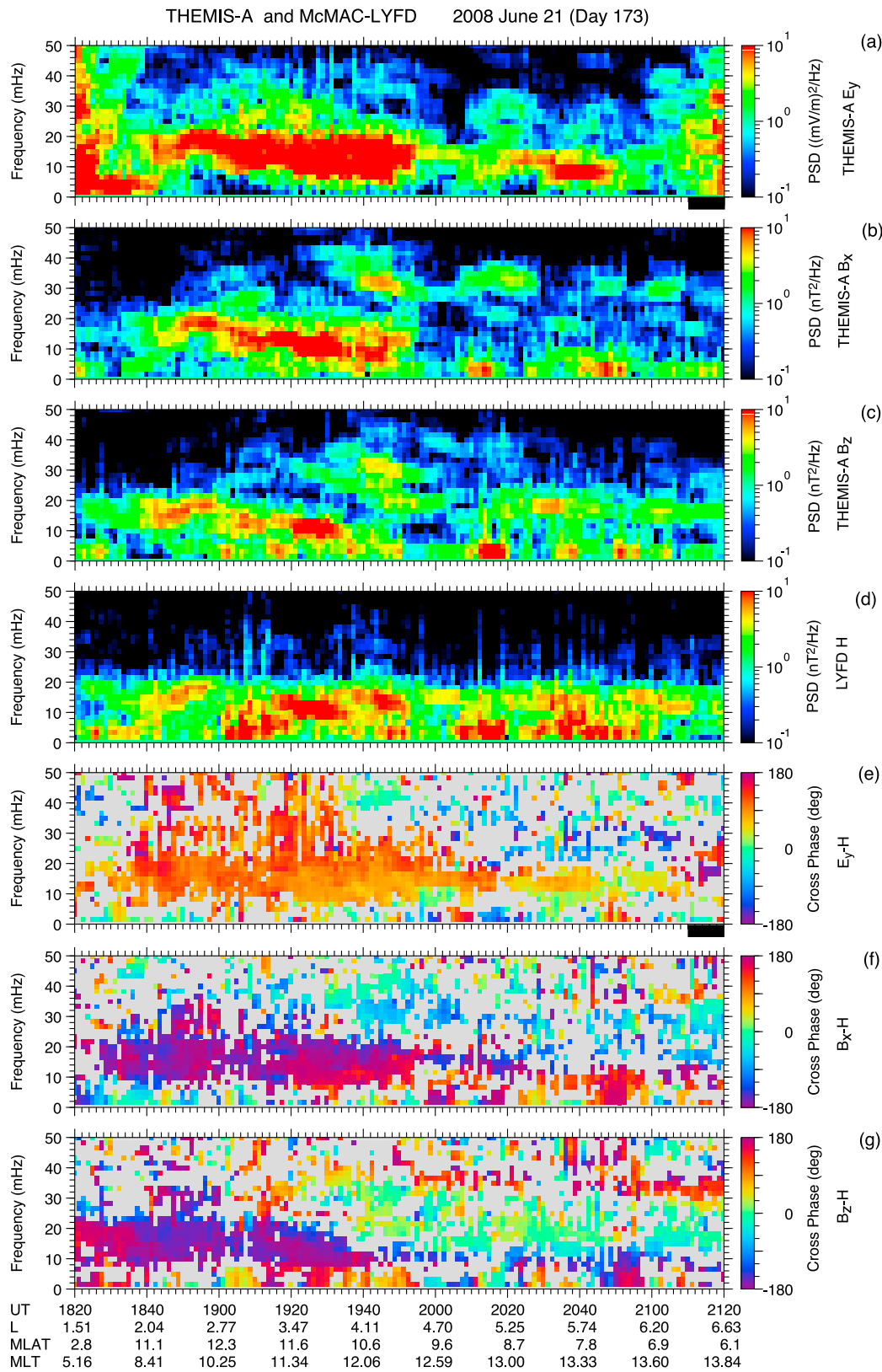
Figure 11. Spectral parameters of the poloidal components E_y, B_x, and B_z at THEMIS-A and the H component at LYFD. A 600 second time window was shifted by 75 seconds in successive steps, with three point smoothing applied in the frequency domain. The spacecraft location is shown at the bottom. (a–d) Power spectral density. (e) Phase of E_y relative to H. (f) Phase of B_x relative to H. (g) Phase of B_z relative to H. The black bar on the time axis for Figures 11a and 11e indicates possible contamination by satellite wake.
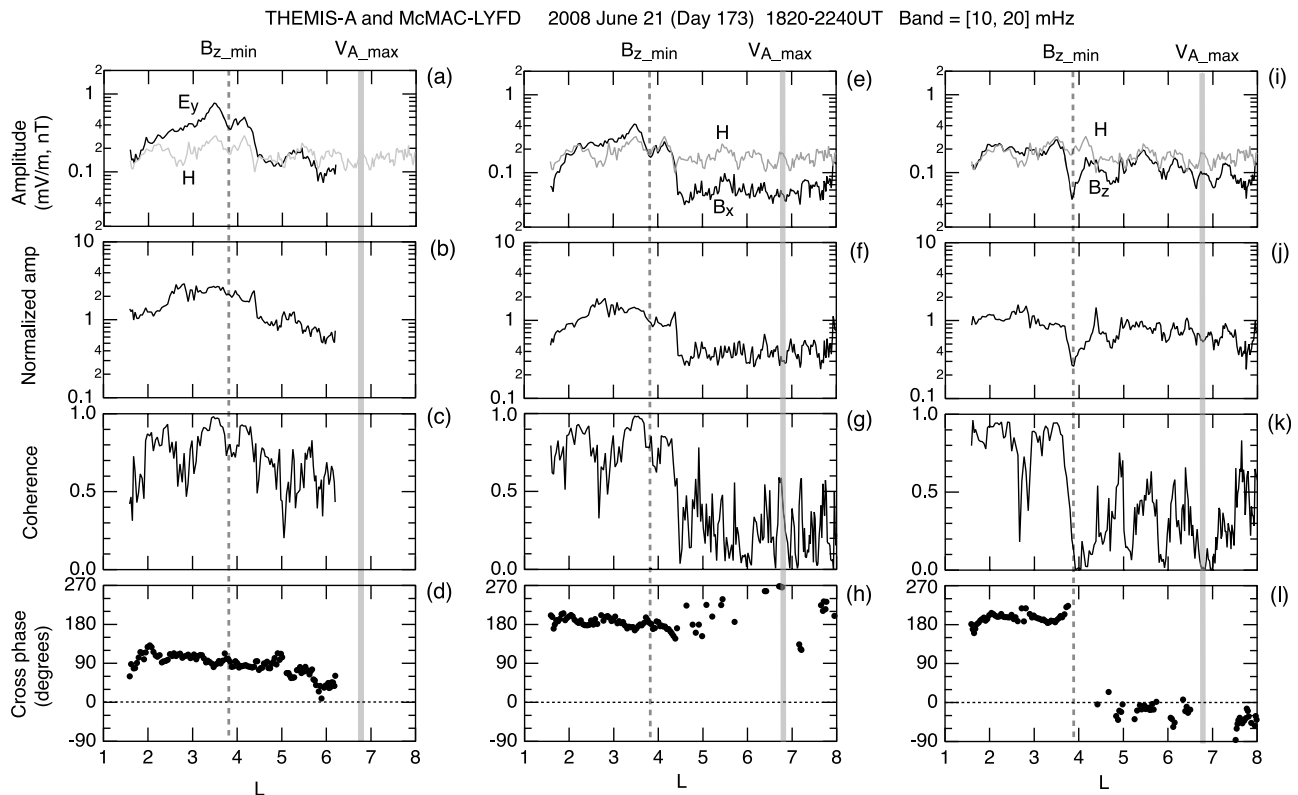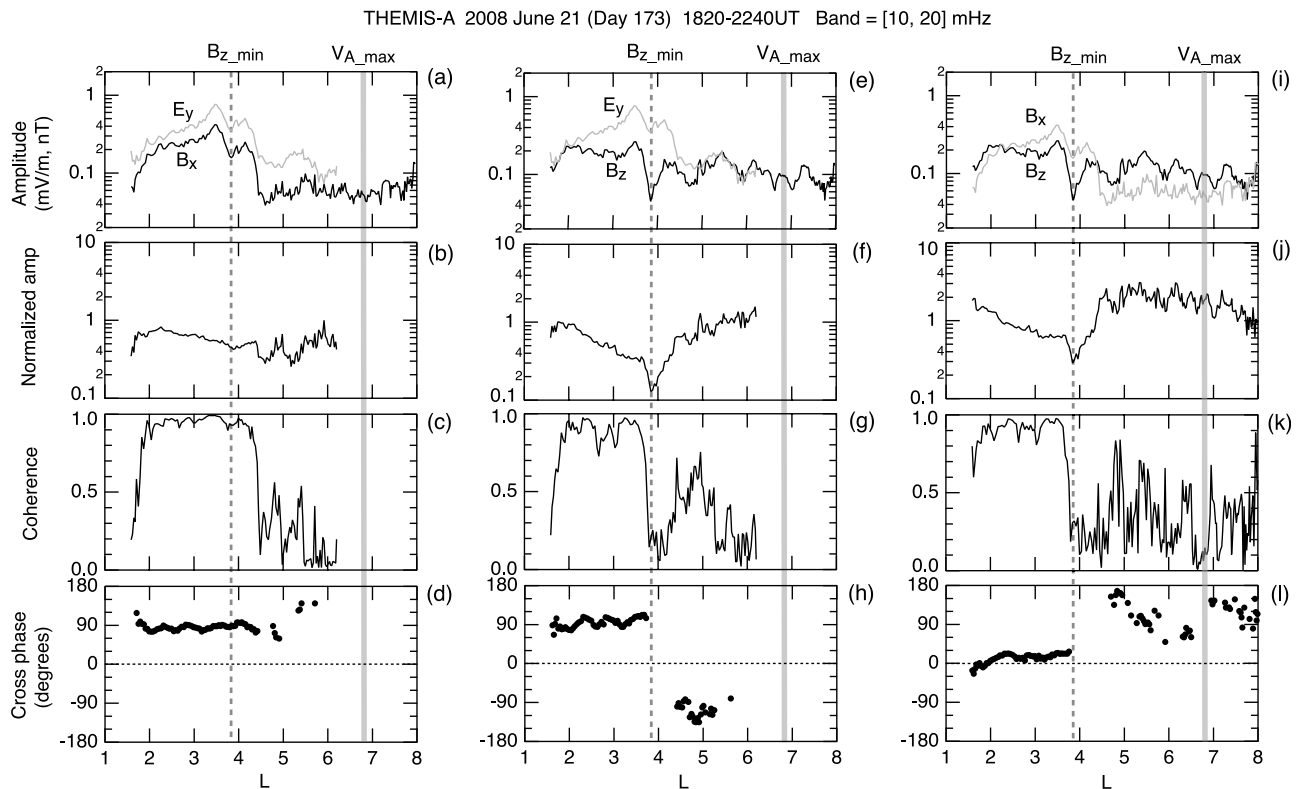
Figure 12. Band-integrated (10–20 mHz) spectral parameters of the poloidal components (a–d) E_y, (e–h) B_x, and (i–l) B_z at THEMIS-A and their comparison with the spectral parameters of the H component at LYFD. All parameters are plotted as a function of L of the spacecraft. E_y data are not plotted for $L > 6.2$ because of possible measurement errors caused by satellite wake. Figures 12a, 12e, and 12i show the raw amplitude. Figures 12b, 12f, and 12j show the amplitude normalized to the H component. Figures 12c, 12g, and 12k show coherence relative to H. Figures 12d, 12h, and 12l show phase relative to H, plotted only if coherence is >0.4. The vertical shaded line at $L = 6.8$ indicates the peak of Alfvén velocity, and the vertical dashed line at $L = 3.8$ indicates the minimum of the B_z amplitude.

band-integrated parameters. Therefore, this technique is suited for extracting essential properties of waves that have a fairly well-defined bandwidth over a long time scale (approximately a few hours) but may change their frequency and amplitude with a short time scale (approximately minutes). The band-integrated parameters are plotted as a function of the dipole L value of THEMIS-A. To make a straightforward comparison with Figure 1c, vertical lines are drawn at the minimum ($L = 3.9$) of the normalized B_z amplitude and at the Alfvén velocity maximum ($L = 6.8$) taken from Figure 9. Also, the cross phase is shown in the range (−90° to 270°) to be consistent with Figure 1c. The reason for this range selection is the fact that the observed B_z-H cross phase is ~180° when the spacecraft is nearest the Earth ($L \sim 1.5$), a feature that is discussed in section 4.4. Note that parameters involving E_y are not shown for $L > 6.2$, where a wake effect made it difficult to evaluate the wave amplitude in the electric field.

[40] In Figure 12a, we find greater variability for E_y than H, suggesting a strong spatial variation of E_y. In fact, the normalized E_y amplitude (Figure 12b) shows a broad but well-defined peak at $L \sim 3.5$, which is within the plasmasphere and close to the location of B_z minimum (or B_z node). The peak value of the normalized E_y amplitude is ~3 (in

units of mV m^{-1} nT^{-1}), which is approximately six times greater than the minimum value of ~0.5 occurring at $L = 6$. This feature can be explained by the trapped fast mode in the plasmasphere (Figure 1b). The cross phase (Figure 12d) remains stable around 90° from $L = 2$ to $L = 5$ with a slow decreasing trend that gives a phase change of ~40° over this distance. This trend mimics the phase of the simulated E_y field shown in Figure 1c. Note that the fast mode propagation time delay from $L = 5$ to $L = 2$ (Tamao's equatorial ToF [*Chi and Russell*, 2005]) is 23 s according to Figure 9c, which translates to a phase delay of ~80° for a 100 s (10 mHz) wave and ~160° for a 50 s (20 mHz) wave. Both are much larger than the observed phase change and make it highly unlikely that the Pc4 pulsations were radially propagating fast mode waves.

[41] The B_x component shows some similarity to E_y but with notable differences. Both the raw (Figure 12e) and normalized (Figure 12f) amplitudes of this component show a broad amplitude maximum around $L \sim 3.5$, quite similar to E_y. However, the amplitude drops abruptly outside $L \sim 4.5$ (Figure 12e), which is qualitatively consistent with the rapid decrease in amplitude seen in the numerical model (Figure 1b) between the amplitude peak and the plasmapause outer edge. As the amplitude drops, the B_x-H coher-

THEMIS-A 2008 June 21 (Day 173) 1820-2240UT Band = [10, 20] mHz

Figure 13. Band-integrated (10–20 mHz) spectral parameters of the poloidal components, (a–d) E_y, (e–h) B_x, and (i–l) B_z at THEMIS-A. All parameters are plotted as a function of L of the spacecraft. E_y data are not plotted for $L > 6.2$ because of possible measurement errors caused by satellite wake. Figures 13a, 13e, and 13i show the raw amplitude of the two components from which the parameters in the second to fourth rows are derived. Figures 13b, 13f, and 13j show the amplitude ratio of the first component (black curve) to the second component (shaded curve). Figures 13c, 13g, and 13k show coherence between the two components. Figures 13d, 13h, and 13l show the phase of the first component relative to the second component, plotted only if coherence is >0.4. The vertical shaded line at $L = 6.8$ indicates the peak of Alfvén velocity, and the vertical dashed line at $L = 3.8$ indicates the minimum of B_z amplitude.

ence (Figure 12g) becomes low, and the B_x-H cross phase (Figure 12h) becomes poorly defined. However, over the L range of appreciable B_x amplitude, the B_x-H cross phase remains near constant consistent with the numerical model shown in Figure 1c.

[42] Plasmaspheric mode trapping also explains the behavior of the B_z component. As we noted in Figure 10d, B_z perturbation during 2015–2030 UT ($L = 3.3$–3.8) was very weak at 13 mHz, when E_y and H oscillations exhibited a strong spectral peak. In Figure 12i, we find that the B_z amplitude had a dip at $L = 3.9$ but the H amplitude did not, indicating that the low B_z intensity at 13 mHz seen in Figure 10d was a spatial rather than a temporal feature. This interpretation is confirmed in the plot of the normalized B_z amplitude (Figure 12j), which shows a clear minimum that is a factor of ~5 deep relative to the surrounding regions $L < 3$ and $L > 5$. At the amplitude minimum, the coherence (Figure 12k) is very low, as expected, and the phase switches by ~180° (Figure 12l). Following Figure 1c, we attribute these features to the crossing of a node of trapped fast mode waves. Taken together, Figures 11 and 12 provide convincing evidence of plasmaspheric mode trapping.

[43] The fact that the phase of E_y relative to H is 90° and that the phase of B_z relative to H is either $-180°$ or 0°

means that E_y and B_z oscillate ±90° out of phase. This in turn means that the x component of the Poynting flux ($= E_yB_z - E_zB_y = E_yB_z$, where E_z is zero by assumption) averaged over a wave period is zero, as should be the case for a radially standing wave. The relationships among E_y, B_x, and B_z in the 10–20 mHz band at THEMIS-A are shown in Figure 13 using the format of Figure 12. E_y and B_x maintained high coherence from $L = 2$ to $L = 4.5$, and in this L range, the cross phase is nearly constant at around 90°. The B_z component also has high coherence with E_y in the low-L region. However, unlike B_x, B_z has a minimum at $L = 3.8$ across which the phase switches by ~180°. The location of these features with respect to the observed plasmapause outer edge (V_{A_min}; see Figure 9) is again consistent with the numerical model shown in Figure 1.

4. Discussion

[44] In this section, we compare our results with those obtained previously on nightside Pi2 pulsations, list similarities and differences between the two phenomena, and identify observations unique to the dayside that warrant further investigation.

4.1. Radial Mode Structure

[45] The radial mode structure of Pc4 pulsations derived in this study (Figures 12 and 13) is qualitatively identical to that obtained for Pi2 pulsations observed on the nightside [*Takahashi et al.*, 1995, 2003]. In these Pi2 studies, the authors constructed the radial mode structure by assembling many events that were observed at various radial distances and used a low-latitude ground magnetometer to normalize the pulsation amplitude in space. In one of these studies [*Takahashi et al.*, 2003], electron number density data were available from the Combined Release and Radiation Effects Satellite (CRRES) and the plasmapause was unambiguously determined. In agreement with our present study, the radial mode structure of the poloidal Pi2 components (E_y, B_x, and B_z) at CRRES was well described by the simulation model shown in Figure 1. On the basis of this comparison, we argue that plasmaspheric mode trapping is a very common phenomenon. Whether one calls a pulsation Pi2 or Pc4 depends on whether it is driven by a short-lived energy source (substorm onset) or by a continuous energy source in the solar wind.

4.2. Frequency

[46] The Pi2 band (period of 40–150 seconds) and Pc4 band (45–150 seconds) are, in practice, the same. These bands were defined empirically based on statistical studies of ground-based observations without addressing specific generation mechanisms [e.g., *Saito*, 1969], and there is no doubt that frequency selection mechanisms other than plasmaspheric trapping exist. However, if we adopt the mode trapping as a major mechanism, then it is straightforward to explain why Pi2 and Pc4 bands overlap. The trapped waves have the mode frequency f_{trap} given by equation (1). The plasmapause density structure is approximately symmetric between night and day [*Moldwin et al.*, 2002], so the trapped waves should exhibit nearly the same frequency both on dayside and nightside under similar solar and geomagnetic conditions.

[47] The two factors that determine f_{trap} are the plasmapause distance L_{pp} and the plasmaspheric Alfvén velocity V_A. In a recent, long-term statistical study of Pi2 pulsations, *Nosé* [2010] found that the Pi2 frequency depends on both the average ion mass M ($=\rho/n_e$) in the plasmasheet and the K_p index. The frequency was higher for lower M and for higher K_p. *Nosé*'s [2010] explanation for these results assumes that the Pi2 pulsations are plasmaspheric trapped mode and that the M value in the plasmasheet is correlated with the M value in the plasmasphere (the F10.7 control of the O^+ production rate at the ionosphere is considered to be the reason for the M variation). It is easy to see how Nosé's scenario works. The average ion mass is related to the Alfvén velocity as $V_A = B_t(\mu_0 n_e M)^{-1/2}$ (low V_A for large M, if n_e remains constant), and K_p controls the plasmapause distance (small L_{pp} for high K_p). These relations, combined with equation (1), explain why the Pi2 frequency depends on M and K_p in the observed manner.

4.3. Energy Source and Its Spectral Property

[48] As we stated in the introduction, a major question pertaining to magnetospheric ULF waves is the relative importance of external forcing and internal resonance in establishing their frequency. In the present analysis, we inferred from the spectral properties of compressional waves observed at GOES that the external driver, the upstream waves, had a frequency close to but slightly higher than the frequency of the Pc4 pulsations observed on the ground and in the plasmasphere. Our interpretation is that the external waves had a finite bandwidth that overlapped the frequency of plasmaspheric trapped waves and that the external waves fed energy to the trapped waves.

[49] The same argument could be made for the frequency selection mechanism of Pi2 pulsations. The concept of trapped fast mode waves has been around for quite some time for Pi2 pulsations [e.g., *Saito and Matsushita*, 1968], and it became the favored interpretation in many more recent studies [e.g., *Yeoman and Orr*, 1989; *Sutcliffe and Yumoto*, 1991]. However, the Pi2 mechanism had a very interesting turn when it was discovered that the temporal variation of the speed of earthward ion bulk flows was similar to low-latitude Pi2 pulsations. This observation led *Kepko and Kivelson* [1999] to suggest that Pi2 pulsations are directly driven by the time-modulated flows, with possible mode conversion as they propagate through the inner magnetosphere [*Kepko et al.*, 2001]. Making an analogy to the relationship between upstream waves and Pc4 that we just discussed, we argue that the oscillatory bulk flows are rarely sinusoidal and thus have a fairly large bandwidth. The plasmaspheric trapped mode can tap energy from the broadband oscillator to establish an eigenfrequency that in general differs from the dominant frequency of the bulk flow oscillations.

[50] This interpretation becomes even more attractive when we realize that the bulk flow waveform observed away from the flow-braking region cannot be the same as that at the braking region. This is simply because the individual flow bursts constituting a wave train reported to date have varying peak speeds. The plasma volumes with fast speed will catch up with plasma volumes with slow speed, and by the time the flow bursts reach the braking region, their waveform should have changed from what was observed farther away (several Earth radii or more). In this case, the waveform matching between low-L Pi2 and flow speed should be considered coincidental rather than causal.

4.4. Phase Delay From Space to Ground

[51] One puzzling observation that we are unable to explain is the phase shift between space and ground associated with the dayside Pc4 pulsations. In nightside observations of Pi2 pulsations, the B_z component earthward of the B_z node (typically located at $L \sim 4$) is in phase with the ground H component at low latitude ($L < 3$) [*Takahashi et al.*, 1995, 1999; *Sutcliffe and Lühr*, 2003; *Han et al.*, 2004]. This Pi2 property was theoretically explained by propagation of fast mode waves from the magnetosphere to the ground through the ionosphere [*Kivelson and Southwood*, 1988; *Allan et al.*, 1996].

[52] In clear contrast to the nightside Pi2 pulsations, our Pc4 pulsations observed in the H component at LYFD near the meridian of THEMIS-A exhibited a phase shift of ~180° with respect to the B_z component observed by the spacecraft inward of the B_z node located at $L = 3.8$ (Figures 11 and 12). We initially suspected a timing error of magnetic field measurements either in space or on the ground, but this

suspicion was quickly dismissed after comparing data from various sources with independent time stamps (e.g., LYFD and Fredericksburg (a U.S. Geological Survey station)) and GOES-11 and THEMIS-A around the time (~2120 UT) of their minimum separation.

[53] Previous studies reported similar phase shifts on the dayside. *Kim and Takahashi* [1999] studied the phase delay of dayside Pc3-4 pulsations (10–30 mHz) observed at the Active Magnetospheric Particle Tracer Explorer/Charge Composition Explorer satellite in the $L = 2$–3 region and on the ground at KAK ($L = 1.3$). High coherence between spacecraft B_z and ground H was observed when the measurements were made within a local time separation of 3 hours. In most of the events, B_z led H by 0°–90°. *Kim and Takahashi* [1999] were unable to explain the phase delay in terms of the ionospheric screening effect as formulated by *Nishida* [1978]. *Jadhav et al.* [2001] examined 10–70 mHz pulsations observed by the Ørsted satellite above low-latitude ($L < 1.5$) ground stations located within 25° of the longitude of the satellite and found that dayside pulsations exhibited a satellite-ground phase shift of 50°–160°. *Jadhav et al.* [2001] argued that the phase shift was introduced at the ionosphere but did not elaborate on the specific mechanism. *Heilig et al.* [2007] reported that a 20–30 mHz pulsation simultaneously observed on the ground at $L = 1.8$ and at the CHAMP satellite (altitude ~ 400 km) with a longitudinal separation of 25° had an ~180° phase shift. *Heilig et al.* [2007] considered this phase shift to be a longitudinal effect. However, for this to be the case, the azimuthal wave number has to be approximately ±7 (equaling ±180°/25°), a value much higher than what we observed (*Heilig et al.* [2007] did not report the value of m for their events).

[54] During 1915–1945 UT, on which the cross-phase analysis shown in Figure 7 was conducted, THEMIS-A and LYFD had a longitudinal separation of ~15°. If we adopt the m value of 1.5 that was determined from the cross-phase analysis presented in Figure 7h between PINE and LOYS for the same time interval, the 15° longitudinal separation would amount to a phase delay of ~22° (= 1.5 × 15°). This estimate is much smaller than the 180° phase shift and leads us to propose that there is some mechanism operating at the ionosphere that introduces the large phase shift.

5. Conclusions

[55] In conclusion, we have presented convincing evidence of mode trapping in the dayside plasmasphere. Well-equipped THEMIS probes provided us with an unprecedented capability to observe in situ the electric and magnetic field perturbations in the inner magnetosphere, including the plasmasphere. This, combined with the use of a magnetoseismic technique to determine the radial variation of the equatorial mass density and the Alfvén velocity, allowed us to compare the observations with theoretical models in great detail. We find excellent agreement between the observations and theoretical models of trapped plasmaspheric waves.

[56] Our analysis also sheds new light on Pi2 pulsations studied using an approach similar to the present one, but with notable differences. The Pi2 mode structure can only be statistically constructed because of the short duration of the nightside pulsations. Also, it is difficult to determine the

mass density radial profile on the nightside because of the absence of continuous toroidal wave activity. We have shown that the mass density plasmasphere has a much larger radial extent than the electron plasmasphere, presumably because of the presence of heavy ions outside of the electron plasmasphere. The wide mass density plasmapause moves the Alfvén velocity peak outward, and as a consequence, the trapping region is radially more extended than the one that is derived from the electron density profile (assuming an H^+ plasma).

[57] Finally, we have presented a possible interpretation of the relationship between Pi2 pulsations and periodic bursty bulk flows by drawing an analogy to the relationship between upstream waves and plasmasphere mode trapping.

References

Allan, W., E. M. Poulter, and S. P. White (1986), Hydromagnetic wave coupling in the magnetosphere: Plasmapause effects on impulse-excited resonances, *Planet. Space Sci.*, *34*, 1189–1220, doi:10.1016/0032-0633 (86)90056-5.

Allan, W., F. W. Menk, B. J. Fraser, Y. Li, and S. P. White (1996), Are low-latitude Pi2 pulsations cavity/waveguide modes?, *Geophys. Res. Lett.*, *23*(7), 765–768, doi:10.1029/96GL00661.

Auster, H. U., et al. (2008), The THEMIS fluxgate magnetometer, *Space Sci. Rev.*, *141*, 235–264, doi:10.1007/s11214-008-9365-9.

Bendat, J. S., and A. G. Piersol (1971), *Random Data: Analysis and Measurement Procedures*, John Wiley, New York.

Björnsson, A., O. Hillebrand, and H. Voelker (1971), First observational results of geomagnetic Pi2 and Pc5 pulsations on a north-south profile through Europe, *Zeit. Geophys.*, *37*, 1031–1042.

Bonnell, J. W., F. S. Mozer, G. T. Delory, A. J. Hull, R. E. Ergun, C. M. Cully, V. Angelopoulos, and P. R. Harvey (2008), The Electric Field Instrument (EFI) for THEMIS, *Space Sci. Rev.*, *141*, 303–341.

Chi, P. J., and C. T. Russell (2005), Travel-time magnetoseismology: Magnetospheric sounding by timing the tremor in space, *Geophys. Res. Lett.*, *32*, L18108, doi:10.1029/2005GL023441.

Clausen, L. B. N., T. K. Yeoman, R. C. Fear, R. Behlke, E. A. Lucek, and M. J. Engebretson (2009), First simultaneous measurements of waves generated at the bow shock in the solar wind, the magnetosphere, and on the ground, *Ann. Geophys.*, *27*, 357–371, doi:10.5194/angeo-27-357-2009.

Cummings, W. D., R. J. O'Sullivan, and P. J. Coleman Jr. (1969), Standing Alfvén waves in the magnetosphere, *J. Geophys. Res.*, *74*(3), 778–793, doi:10.1029/JA074i003p00778.

Denton, R. E. (2006), Magnetoseismology using spacecraft observations, in *Magnetospheric ULF Waves: Synthesis and New Directions*, edited by K. Takahashi et al., pp. 307–317, AGU, Washington, D. C.

Denton, R. E., D.-H. Lee, K. Takahashi, J. Goldstein, and R. Anderson (2002), Quantitative test of the cavity resonance explanation of plasmaspheric Pi2 frequencies, *J. Geophys. Res.*, *107*(A7), 1093, doi:10.1029/2001JA000272.

Denton, R. E., K. Takahashi, R. R. Anderson, and M. P. Wuest (2004), Magnetospheric toroidal Alfvén wave harmonics and the field line distribution of mass density, *J. Geophys. Res.*, *109*, A06202, doi:10.1029/2003JA010201.

Denton, R. E., K. Takahashi, I. A. Galkin, P. A. Nsumei, X. Huang, B. W. Reinisch, R. R. Anderson, M. K. Sleeper, and W. J. Hughes (2006), Distribution of density along magnetospheric field lines, *J. Geophys. Res.*, *111*, A04213, doi:10.1029/2005JA011414.

Engebretson, M. J., L. J. Zanetti, T. A. Potemra, and M. H. Acuña (1986), Harmonically structured ULF pulsations observed by the AMPTE CCE magnetic field experiment, *Geophys. Res. Lett.*, *13*(9), 905–908, doi:10.1029/GL013i009p00905.

Fairfield, D. H. (1969), Bow shock associated waves observed in the far upstream interplanetary medium, *J. Geophys. Res.*, *74*(14), 3541–3553, doi:10.1029/JA074i014p03541.

Feng, Q., B. J. Fraser, F. W. Menk, C. W. S. Ziesolleck, O. Saka, and T. Kitamura (1995), Pc3-4 geomagnetic pulsations observed at very low latitude conjugate stations, *J. Geophys. Res.*, *100*(A10), 19,287–19,298, doi:10.1029/94JA01260.

Fraser, B. J., J. L. Horwitz, J. A. Slavin, Z. C. Dent, and I. R. Mann (2005), Heavy ion mass loading of the geomagnetic field near the plasmapause and ULF wave implications, *Geophys. Res. Lett.*, *32*, L04102, doi:10.1029/2004GL021315.

Fujita, S., and K. H. Glassmeier (1995), Magnetospheric cavity resonance oscillations with energy flow across the magnetopause, *J. Geomag. Geoelectr.*, *47*, 1277–1292.

Fujita, S., H. Nakata, M. Itonaga, A. Yoshikawa, and T. Mizuta (2002), A numerical simulation of the Pi2 pulsations associated with the substorm current wedge, *J. Geophys. Res.*, *107*(A3), 1034, doi:10.1029/2001JA900137.

Greenstadt, E. W., and J. V. Olson (1976), Pc3, 4 activity and interplanetary field orientation, *J. Geophys. Res.*, *81*(34), 5911–5920, doi:10.1029/JA081i034p05911.

Han, D. S., T. Iyemori, M. Nosé, H. McCreadie, Y. Gao, F. Yang, S. Yamashita, and P. Stauning (2004), A comparative analysis of low-latitude Pi2 pulsations observed by Ørsted and ground stations, *J. Geophys. Res.*, *109*, A10209, doi:10.1029/2004JA010576.

Heilig, B., H. Lühr, and M. Rother (2007), Comprehensive study of ULF upstream waves observed in the topside ionosphere by CHAMP and on the ground, *Ann. Geophys.*, *25*, 737–754.

Howard, T. A., and F. W. Menk (2001), Propagation of 10–50 mHz ULF waves with high spatial coherence at high latitudes, *Geophys. Res. Lett.*, *28*(2), 231–234, doi:10.1029/2000GL011993.

Jadhav, G., M. Rajaram, and R. Rajaram (2001), Modification of daytime compressional waves by the ionosphere: First results from OERSTED, *Geophys. Res. Lett.*, *28*(1), 103–106, doi:10.1029/2000GL011940.

Kepko, L., and M. Kivelson (1999), Generation of Pi2 pulsations by bursty bulk flows, *J. Geophys. Res.*, *104*(A11), 25,021–25,034, doi:10.1029/1999JA900361.

Kepko, L., M. G. Kivelson, and K. Yumoto (2001), Flow bursts, braking, and Pi2 pulsations, *J. Geophys. Res.*, *106*, 1903–1915, doi:10.1029/2000JA000158.

Kepko, L., H. E. Spence, and H. J. Singer (2002), ULF waves in the solar wind as direct drivers of magnetospheric pulsations, *Geophys. Res. Lett.*, *29*(8), 1197, doi:10.1029/2001GL014405.

Kim, K. H., and K. Takahashi (1999), Statistical analysis of compressional Pc3-4 pulsations observed by AMPTE CCE at *L* = 2–3 in the dayside magnetosphere, *J. Geophys. Res.*, *104*(A3), 4539–4558, doi:10.1029/1998JA900131.

Kim, K. H., K. Takahashi, and B. J. Anderson (1998), Ground-satellite coherence analysis of Pc3 pulsations, *J. Geophys. Res.*, *103*(A6), 11,755–11,769, doi:10.1029/98JA00617.

Kivelson, M. G., and D. J. Southwood (1988), Hydromagnetic waves and the ionosphere, *Geophys. Res. Lett.*, *15*(11), 1271–1274, doi:10.1029/GL015i011p01271.

Kivelson, M. G., J. Etcheto, and J. G. Trotignon (1984), Global compressional oscillations of the terrestrial magnetosphere: The evidence and a model, *J. Geophys. Res.*, *89*(A11), 9851–9856, doi:10.1029/JA089i011p09851.

Klimushkin, D. Y., P. N. Mager, and K.-H. Glassmeier (2004), Toroidal and poloidal Alfvén waves with arbitrary azimuthal wave numbers in a finite pressure plasma in the Earth's magnetosphere, *Ann. Geophys.*, *22*, 267–287.

Krauss-Varban, D. (1994), Bow shock and magnetosheath simulations: Wave transport and kinetic properties, in *Solar Wind Sources of Magnetospheric Ultra-Low Frequency Waves, Geophys. Monogr. Ser.*, vol. 81, edited by M. J. Engebretson et al., pp. 121–134, AGU, Washington, D. C.

Le, G., and C. T. Russell (1992), A study of ULF wave foreshock morphology: II. Spatial variation of ULF waves, *Planet. Space Sci.*, *40*, 1227–1234.

Lee, D.-H. (1998), On the generation mechanism of Pi2 pulsations in the magnetosphere, *Geophys. Res. Lett.*, *25*(5), 583–586, doi:10.1029/98GL50239.

Lee, D.-H., and K. Kim (1999), Compressional MHD waves in the magnetosphere: A new approach, *J. Geophys. Res.*, *104*(A6), 12,379–12,385, doi:10.1029/1999JA900053.

Lee, D.-H., and R. L. Lysak (1989), Magnetospheric ULF Wave Coupling in the Dipole Model: the Impulsive Excitation, *J. Geophys. Res.*, *94*(A12), 17,097–17,103, doi:10.1029/JA094iA12p17097.

Lee, D.-H., and R. L. Lysak (1999), MHD waves in a three-dimensional dipolar magnetic field: A search for Pi2 pulsations, *J. Geophys. Res.*, *104*(A12), 28,691–28,699, doi:10.1029/1999JA900377.

Leonovich, A. S., and V. A. Mazur (2000a), Structure of magnetosonic eigenoscillations of an axisymmetric magnetosphere, *J. Geophys. Res.*, *105*(A12), 27,707–27,715, doi:10.1029/2000JA000108.

Leonovich, A. S., and V. A. Mazur (2000b), Toward the theory of magnetospheric magnetosonic eigenoscillations: Simple theoretical models, *J. Geophys. Res.*, *105*(A9), 21,251–21,260, doi:10.1029/1999JA000399.

Leonovich, A. S., and V. A. Mazur (2001), On the spectrum of magnetosonic eigenoscillations of an axisymmetric magnetosphere, *J. Geophys. Res.*, *106*, 3919–3927, doi:10.1029/2000JA000228.

Li, W., et al. (2010), THEMIS analysis of observed equatorial electron distributions responsible for the chorus excitation, *J. Geophys. Res.*, *115* A00F11, doi:10.1029/2009JA014845.

Menk, F. W., D. Orr, M. A. Clilverd, A. J. Smith, C. L. Waters, D. K. Milling, and B. J. Fraser (1999), Monitoring spatial and temporal variations in the dayside plasmasphere using geomagnetic field line resonances, *J. Geophys. Res.*, *104*(A9), 19,955–19,969, doi:10.1029/1999JA900205.

Moldwin, M. B., L. Downward, H. K. Rassoul, R. Amin, and R. R. Anderson (2002), A new model of the location of the plasmapause: CRRES results, *J. Geophys. Res.*, *107*(A11), 1339, doi:10.1029/2001JA009211.

Mozer, F. S. (1974), Analysis of techniques for measuring DC and AC electric fields in the magnetosphere, *Space Sci. Rev.*, *14*, 272–313.

Newton, R. S., D. J. Southwood, and W. J. Hughes (1978), Damping of geomagnetic pulsations by the ionosphere, *Planet. Space Sci.*, *26*, 201–209.

Nishida, A. (1978), *Geomagnetic Diagnosis of the Magnetosphere*, Springer, New York.

Nosé, M. (2010), Excitation mechanism of low-latitude Pi2 pulsations: Cavity mode resonance or BBF-driven process?, *J. Geophys. Res.*, *115*, A07221, doi:10.1029/2009JA015205.

O'Brien, T. P., and M. B. Moldwin (2003), Empirical plasmapause models from magnetic indices, *Geophys. Res. Lett.*, *30*(4), 1152, doi:10.1029/2002GL016007.

Odera, T. J., D. Van Swol, C. T. Russell, and C. A. Green (1991), Pc3,4 magnetic pulsations observed simultaneously in the magnetosphere and at multiple ground stations, *Geophys. Res. Lett.*, *18*(9), 1671–1674, doi:10.1029/91GL01297.

Pekrides, H., A. D. M. Walker, and P. R. Sutcliffe (1997), Global modeling of Pi2 pulsations, *J. Geophys. Res.*, *102*(A7), 14,343–14,354, doi:10.1029/97JA00747.

Ponomarenko, P. V., F. M. Menk, C. L. Waters, and M. D. Sciffer (2005), Pc3-4 ULF waves observed by the SuperDARN TIGER radar, *Ann. Geophys.*, *23*, 1271–1280.

Poulter, E. M., and E. Nielsen (1982), The hydromagnetic oscillation of individual shells, *J. Geophys. Res.*, *87*(A12), 10,432–10,438, doi:10.1029/JA087iA12p10432.

Price, I. A., C. L. Waters, F. W. Menk, G. J. Bailey, and B. J. Fraser (1999), A technique to investigate plasma mass density in the topside ionosphere using ULF waves, *J. Geophys. Res.*, *104*(A6), 12,723–12,732, doi:10.1029/1999JA900042.

Radoski, H. R. (1967), Highly asymmetric MHD resonances: The guided poloidal mode, *J. Geophys. Res.*, *72*(15), 4026–4027, doi:10.1029/JZ072i015p04026.

Russell, C. T., P. J. Chi, D. J. Dearborn, Y. S. Ge, B. Kuo-Tiong, J. D. Means, D. R. Pierce, K. M. Rowe, and R. C. Snare (2008), THEMIS ground-based magnetometers, *Space Sci. Rev.*, *141*, 389–412, doi:10.1007/s11214-008-9337-0.

Saito, T. (1969), Geomagnetic pulsations, *Space Sci. Rev.*, *10*, 319–412.

Saito, T., and S. Matsushita (1968), Solar cycle effects on geomagnetic Pi2 pulsations, *J. Geophys. Res.*, *73*(1), 267–286, doi:10.1029/JA073i001p00267.

Samson, J. C., B. G. Harrold, J. M. Ruohoniemi, R. A. Greenwald, and A. D. M. Walker (1992), Field line resonance associated with MHD waveguides in the magnetosphere, *Geophys. Res. Lett.*, *19*(5), 441–444, doi:10.1029/92GL00116.

Schäfer, S., K. H. Glassmeier, P. T. I. Eriksson, V. Pierrard, K. H. Fornaçon, and L. G. Blomberg (2007), Spatial and temporal characteristics of poloidal waves in the terrestrial plasmasphere: A Cluster case study, *Ann. Geophys.*, *25*, 1011–1024.

Schäfer, S., K. H. Glassmeier, P. T. I. Eriksson, P. N. Mager, V. Pierrard, K. H. Fornaçon, and L. G. Blomberg (2008), Spatiotemporal structure of a poloidal Alfvén wave detected by Cluster adjacent to the dayside plasmapause, *Ann. Geophys.*, *26*, 1805–1817.

Sibeck, D. G., and V. Angelopoulos (2008), THEMIS science objectives and mission phases, *Space Sci. Rev.*, *141*, 33–59, doi:10.1007/s11214-008-9393-5.

Singer, H. J., D. J. Southwood, R. J. Walker, and M. G. Kivelson (1981), Alfvén wave resonances in a realistic magnetospheric magnetic field geometry, *J. Geophys. Res.*, *86*(A6), 4589–4596, doi:10.1029/JA086iA06p04589.

Singer, H. J., L. Matheson, R. Grubb, A. Newman, and S. D. Bouwer (1996), Monitoring space weather with the GOES magnetometers, in *GOES-8 and Beyond*, *Proc. SPIE Int. Soc. Opt. Eng.*, vol. 2812, edited by E. R. Washwell, pp. 299–308.

Sutcliffe, P. R., and H. Lühr (2003), A comparison of Pi2 pulsations observed by CHAMP in low Earth orbit and on the ground at low latitudes, *Geophys. Res. Lett.*, *30*(21), 2105, doi:10.1029/2003GL018270.

Sutcliffe, P. R., and K. Yumoto (1991), On the cavity mode nature of low-latitude Pi2 pulsations, *J. Geophys. Res.*, *96*(A2), 1543–1551, doi:10.1029/90JA02007.

Takahashi, K., R. L. McPherron, and T. Terasawa (1984a), Dependence of the spectrum of Pc3-4 pulsations on the interplanetary magnetic field, *J. Geophys. Res.*, *89*(A5), 2770–2780, doi:10.1029/JA089iA05p02770.

Takahashi, K., R. L. McPherron, and W. J. Hughes (1984b), Multispacecraft observations of the harmonic structure of Pc3-4 magnetic pulsations, *J. Geophys. Res.*, *89*(A8), 6758–6774, doi:10.1029/JA089iA08p06758.

Takahashi, K., S. Ohtani, and B. J. Anderson (1995), Statistical analysis of Pi2 pulsations observed by the AMPTE CCE spacecraft in the inner magnetosphere, *J. Geophys. Res.*, *100*(A11), 21,929–21,941, doi:10.1029/95JA01849.

Takahashi, K., B. J. Anderson, and K. Yumoto (1999), Upper atmosphere research satellite observation of a Pi2 pulsation, *J. Geophys. Res.*, *104*(A11), 25,035–25,045, doi:10.1029/1999JA900317.

Takahashi, K., D. H. Lee, M. Nosé, R. R. Anderson, and W. J. Hughes (2003), CRRES electric field study of the radial mode structure of Pi2 pulsations, *J. Geophys. Res.*, *108*(A5), 1210, doi:10.1029/2002JA009761.

Takahashi, K., R. E. Denton, R. R. Anderson, and W. J. Hughes (2006), Mass density inferred from toroidal wave frequencies and its comparison to electron density, *J. Geophys. Res.*, *111*, A01201, doi:10.1029/2005JA011286.

Takahashi, K., D. Berube, D.-H. Lee, J. Goldstein, H. J. Singer, and F. Honary (2009), Possible evidence of virtual resonance in the dayside magnetosphere, *J. Geophys. Res.*, *114*, A05206, doi:10.1029/2008JA013898.

Takahashi, K., R. E. Denton, and H. J. Singer (2010), Solar cycle variation of geosynchronous plasma mass density derived from the frequency of standing Alfvén waves, *J. Geophys. Res.*, *115*, A07207, doi:10.1029/2009JA015243.

Tamao, T. (1978), Coupling modes of hydromagnetic oscillations in non-uniform, finite pressure plasmas: Two-fluids model, *Planet. Space Sci.*, *26*, 1141–1148.

Troitskaya, V. A., T. A. Plyasova-Bakounina, and A. V. Gul'yel'mi (1971), Relationship between Pc2-4 pulsations and the interplanetary magnetic field, *Dokl. Akad. Nauk SSSR*, *197*, 1312–1314.

Tsunomura, S., A. Yamazaki, T. Tokumoto, and Y. Yamada (1994), The new system of Kakioka automatic standard magnetometer, *Mem. Kakioka Mag. Obs.*, *25*, 3–32.

Tsyganenko, N. A. (1989), A magnetospheric magnetic field model with a warped tail current sheet, *Planet. Space Sci.*, *37*, 5–20.

Tsyganenko, N. A., and M. I. Sitnov (2005), Modeling the dynamics of the inner magnetosphere during strong geomagnetic storms, *J. Geophys. Res.*, *110*, A03208, doi:10.1029/2004JA010798.

Turkakin, H., R. Marchand, and Z. C. Kale (2008), Mode trapping in the plasmasphere, *J. Geophys. Res.*, *113*, A11210, doi:10.1029/2008JA013045.

Vellante, M., U. Villante, M. De Lauretis, and G. Barchi (1996), Solar cycle variation of the dominant frequencies of Pc3 geomagnetic pulsations at $L = 1.6$, *Geophys. Res. Lett.*, *23*(12), 1505–1508, doi:10.1029/96GL01399.

Yeoman, T. K., and D. Orr (1989), Phase and spectral power of midlatitude Pi2 pulsations: Evidence for a plasmaspheric cavity resonance, *Planet. Space Sci.*, *37*, 1367–1383.

Yumoto, K., and T. Saito (1983), Relation of compressional HM waves at GOES 2 to low-latitude Pc3 magnetic pulsations, *J. Geophys. Res.*, *88*(A12), 10,041–10,052, doi:10.1029/JA088iA12p10041.

Yumoto, K., A. Isono, K. Shiokawa, H. Matsuoka, Y. Tanaka, F. W. Menk, B. J. Fraser, M. J. Engebretson, K. Takahashi, and M. Scholer (1994), Global cavity mode-like and localized field line Pc3-4 oscillations stimulated by interplanetary impulses (si/sc): Initial results from the 210° MM magnetic observations, in *Solar Wind Sources of Magnetospheric Ultra-Low-Frequency Waves*, *Geophys. Monogr. Ser.*, vol. 81, edited by M. Engebretson et al., pp. 335–344, AGU, Washington, D. C.

Ziesolleck, C. W. S., B. J. Fraser, F. W. Menk, and P. W. McNabb (1993), Spatial characteristics of low-latitude Pc3-4 geomagnetic pulsations, *J. Geophys. Res.*, *98*(A1), 197–207, doi:10.1029/92JA01433.

Zhu, X., and M. G. Kivelson (1989), Global mode ULF pulsations in a magnetosphere with a nonmonotonic Alfvén velocity profile, *J. Geophys. Res.*, *94*(A2), 1479–1485, doi:10.1029/JA094iA02p01479.

V. Angelopoulos and P. J. Chi, Institute of Geophysics and Planetary Physics, University of California, 100 Stein Plaza, Los Angeles, CA 90095-7065, USA.

J. Bonnell, Space Sciences Laboratory, University of California, 7 Gauss Way, Berkeley, CA 94720-7450, USA.

R. E. Denton, Department of Physics and Astronomy, Dartmouth College, Hanover, NH 03755-3528, USA.

K.-H. Glassmeier, Institut für Geophysik und Extraterrestrische Physik, Technical University of Braunschweig, Mendelssohnstr. 3, D-38106, Braunschweig, Germany.

D.-H. Lee, School of Space Research, Kyung Hee University, Yongin, KR-446-701 Gyeonggi, South Korea.

W. Liu, Laboratory for Atmospheric and Space Physics, University of Colorado at Boulder, 1234 Innovation Dr., Boulder, CO 80303-7814, USA.

Y. Nishimura, Department of Atmospheric and Oceanic Sciences, University of California, 100 Stein Plaza, Los Angeles, CA 90095-7065, USA.

M. Nosé, Data Analysis Center for Geomagnetism and Space Magnetism, Graduate School of Science, Kyoto University, Kitashirakawa-Oiwake Cho, Sakyo-ku, Kyoto 606-8502, Japan.

H. J. Singer, National Oceanic and Atmospheric Administration/National Weather Service, National Centers for Environmental Prediction, Space Weather Prediction Center, 325 Broadway, Boulder, CO 80305, USA.

K. Takahashi, Johns Hopkins University Applied Physics Laboratory, 11100 Johns Hopkins Rd., Laurel, MD 20723, USA. (kazue.takahashi@jhuapl.edu)